A ground-to-exosphere Martian general circulation model: 1. Seasonal, diurnal, and solar cycle variation of thermospheric temperatures

F. González-Galindo,[1] F. Forget,[1] M. A. López-Valverde,[2] M. Angelats i Coll,[1] and E. Millour[1]

Received 4 August 2008; revised 21 November 2008; accepted 18 December 2008; published 1 April 2009.

[1] We present the extension to the thermosphere of a Martian general circulation model, the first able to self-consistently study the whole Martian atmosphere from the surface to the exosphere. We describe the parameterizations developed to include physical processes important for thermospheric altitudes. The results of a simulation covering 1 full Martian year are presented, focusing on the seasonal, diurnal, and day-to-day variability of the temperatures in the exobase region. The seasonal variation of the zonal mean temperatures in the upper atmosphere is of about 100 K, mostly due to the variation of the solar forcing. The temperature of the mesopause ranges between 115 and 130 K, with little seasonal and day-night variations. Its pressure level undergoes significant seasonal and day-night variations. Comparisons with SPICAM observations show that the modeled mesopause is too low and too warm. A similar study for the homopause shows that it is located higher in the atmosphere during solstices, owing to reinforced mixing by a stronger circulation. Important day-night temperature differences are found in the thermosphere, ranging from about 60 K at aphelion to 110 K at perihelion. This diurnal cycle is slightly perturbed by the day-to-day variations of temperature, dominated by waves with periods of 2 to 6 sols and amplitude of 30 K. The model reproduces the observed solar cycle variation in temperatures when using a UV heating efficiency of 16%, slightly lower than the theoretical value. The seasonal variation of temperatures is overestimated by the model, in comparison with the available measurements.

Citation: González-Galindo, F., F. Forget, M. A. López-Valverde, M. Angelats i Coll, and E. Millour (2009), A ground-to-exosphere Martian general circulation model: 1. Seasonal, diurnal, and solar cycle variation of thermospheric temperatures, *J. Geophys. Res.*, *114*, E04001, doi:10.1029/2008JE003246.

1. Introduction

[2] During the last 40 years, the international effort of exploration and the increasing complexity of theoretical models have been the two fundamental drivers for our steps toward a more complete description of the Martian atmosphere. Owing to the inherent difficulty of observation of the upper atmosphere, most of these efforts have focused on the lower atmosphere, and little data have been obtained on the upper regions. However, during the last decade a renewed interest on the upper Martian atmosphere has grown. In this work, we will use the term "upper atmosphere" to refer to the mesosphere and thermosphere, i.e., those layers above approximately 60 km.

[3] Different missions have sounded this region, retrieving a significant amount of information. A common point to all these observations is that they show an important coupling between the lower and the upper atmosphere. Some examples are presented below.

[4] During its aerobraking phases, Mars Global Surveyor accelerometers measured the atmospheric drag, retrieving densities in the lower thermosphere. A longitudinal variation, mainly composed of wave numbers 2 and 3 was found [*Keating et al.*, 1998]. Although first attributed to stationary waves, further studies showed that nonmigrating waves, arising through the interaction between the solar illumination and the topography, and by nonlinear interactions between waves, were at the origin of the observed structures [e.g., *Wilson*, 2000, 2002; *Forbes et al.*, 2002; *Angelats i Coll et al.*, 2004]. A sudden increase of thermospheric density coincident with a dust storm in the lower atmosphere was also found [*Keating et al.*, 1998].

[5] Also during its aerobraking phase, Mars Odyssey detected for the first time an increase of temperature in the lower thermosphere when going into the polar night during perihelion season (i.e., northern winter) [*Keating et al.*, 2003]. A polar warming had already been observed in the lower atmosphere and theoretically explained by models

[1] Laboratoire de Météorologie Dynamique, Institute Pierre Simon Laplace, Paris, France.
[2] Instituto de Astrofísica de Andalucía, CSIC, Granada, Spain.

Copyright 2009 by the American Geophysical Union.
0148-0227/09/2008JE003246

[*Wilson*, 1997; *Forget et al.*, 1999], but it had never been observed in the thermosphere. For the opposite season (southern winter), the aerobraking observations by MGS and MRO show a much weaker warming or even no warming at all [*Keating et al.*, 2007]. The origin of this increase of temperature is the adiabatic warming induced by the convergence and downwelling of air from the upper thermosphere in the polar winter region, owing to an enhanced interhemispheric transport at perihelion [*Bougher et al.*, 2006]. *Bell et al.* [2007] have shown that the intensity of the thermospheric polar warming predicted by the Mars Thermospheric General Circulation Model (MTGCM) is affected by the amount and vertical distribution of the dust in the lower atmosphere.

[6] SPICAM on board Mars Express is providing very valuable information about the upper atmosphere. Its UV spectrometer has detected for the first time on Mars nighttime emissions by NO [*Bertaux et al.*, 2005]. Peak emissions are found between about 55 and 95 km of altitude, although no clear trend of the peak intensity or altitude with latitude, longitude, local time or solar activity has been identified [*Cox et al.*, 2008]. These emissions originate in the recombination of nitrogen and oxygen atoms, which are produced by photodissociation of CO_2, O_2 and N_2 in the dayside upper thermosphere, and then transported to the nightside mesosphere/lower thermosphere. SPICAM stellar occultation technique has also allowed for a systematic sounding of the Martian atmosphere between 60 and 130 km, retrieving density and temperature profiles [*Forget et al.*, 2009]. A sudden increase of density is found around L_s = 130 that is related to an unusual dust storm event. A polar warming in the southern winter at altitudes between 70 and 100 km is also found.

[7] All these observations unveil a very complex and dynamically rich upper atmosphere, strongly affected by the interactions with other regions and between different radiative, chemical and dynamical processes. In order to achieve a complete understanding of the upper atmosphere, it is very important to include all atmospheric regions and to take into account these couplings.

[8] On the modeling side, many efforts have been put in the development of general circulation models (GCMs) for Mars, but most of them are devoted to the study of the lower atmosphere. The only thermospheric Martian GCM until recently was the Mars Thermospheric GCM [*Bougher et al.*, 1990, 1999a, 2000]. Although it is a purely thermospheric model (that is, it does not include the lower atmosphere), in the last years it has been coupled to the NASA/Ames MGCM to account for the effects of the lower atmosphere. This coupling captured upward propagating migrating and nonmigrating tides, but no downward coupling is enabled [*Bougher et al.*, 2006]. These coupled GCMs have been successfully applied in a number of studies of the Martian thermosphere, like the analysis of electron density profiles of MGS [*Bougher et al.*, 2004], the MGS density structures [*Bougher et al.*, 1999b], the thermospheric polar warming [*Bougher et al.*, 2006; *Bell et al.*, 2007], and mesopause temperatures (T. McDunn et al., Simulating the density and thermal structure of the middle atmosphere (≈70–130 km) of Mars using the MGCM-MTGCM: A comparison with MEX-SPICAM observations, submitted to *Icarus*, 2008).

[9] A different strategy has been followed in the Laboratoire de Météorologie Dynamique (LMD, Paris, France) to study the upper atmosphere and the important couplings with the lower regions. The existing GCM for the Martian lower atmosphere [*Hourdin et al.*, 1993; *Forget et al.*, 1999] has been extended up to the thermosphere, in an international collaboration with the Instituto de Astrofísica de Andalucía (Granada, Spain). In this way, the LMD-MGCM has become the first single Martian GCM able to study self-consistently the whole atmospheric range, from the surface to the upper thermosphere. This strategy has some intrinsic advantages because the couplings and feedbacks between layers are naturally included and do not need to be treated as boundary conditions; also a consistent radiative transfer is used, eliminating differences in radiative schemes between coupled models. The idea of extending a single GCM to span the Mars lower and upper atmospheres is under active consideration in other groups [*Crowley et al.*, 2003; *Ridley et al.*, 2004; *Moudden and McConnell*, 2005; *Bougher et al.*, 2008].

[10] In this paper, we present the extension of the LMD-MGCM to the thermosphere in section 2, and the input data used for the simulations presented in section 3. Some studies made with this extended model are presented. In particular, the seasonal latitudinal and vertical variations of upper atmospheric temperatures are presented in section 4. Additionally, the altitude of two critical levels, the mesopause and the homopause, is also studied in section 4. In section 5 we compare the day-to-day variability of the temperatures with its day-night variation and the seasonal variation. The variability with the solar cycle is studied in section 6.

2. Model Description

[11] The model presented here is the extension to the thermosphere of the GCM described by *Forget et al.* [1999] (hereafter referred as paper 1), which includes the most relevant processes in the 0–80 km altitude range. In short, the model solves the primitive equations of hydrodynamics in a sphere, using a grid point discretization. The radiative balance accounts for the effect of CO_2 and suspended dust. A realistic CO_2 condensation scheme is included, essential for a good simulation of the surface pressure annual cycle. A water cycle [*Montmessin et al.*, 2004] and a photochemical model for the lower atmosphere [*Lefevre et al.*, 2004] have also been included in the model. A number of subgrid-scale processes near the surface are considered, in particular the boundary layer turbulence, convection, relief drag and gravity wave drag. An improvement with respect to the model described in paper 1 is the updating of surface properties provided by MGS, in particular MOLA topography and TES thermal inertia. This improves the comparison with observations in the lower atmosphere, but has no significant effect on the upper atmosphere.

[12] 14 chemical species are included in the model: CO_2, CO, $O(^3P)$, $O(^1D)$, O_2, O_3, H, OH, HO_2, H_2, H_2O, H_2O_2, N_2 and Ar. All of them undergo the transport by the general circulation, as well as by molecular diffusion, as we will see below. N_2 and Ar are treated as chemically inert, while all the other species are affected by chemistry, as we will see later.

[13] The extension to the thermosphere was briefly presented before by *Angelats i Coll et al.* [2005]. Here we describe it in detail.

[14] A two-step approach was used to extend the LMD-MGCM up to the thermosphere. First, the model was extended up to about 120 km by adding NLTE corrections to the CO_2 IR radiative balance. This allowed us to compare the results of the model with the density measured during the MGS aerobraking and to confirm the role of diurnal Kelvin waves in creating the wave structure observed by the spacecraft [*Angelats i Coll et al.*, 2004]. Second, the model was extended up to the thermosphere (with an upper limit at about 250 km) by adding physical processes specific of these altitudes: UV heating, thermal conduction, molecular diffusion and a photochemical model appropriate for the upper atmosphere. As usual in a GCM, the CPU time consumption is an important constraint, so fast parameterizations and approximations had to be developed to make these processes suitable for a GCM. We describe the implementation of these processes below.

2.1. NLTE Corrections to CO_2 Radiative Balance

[15] CO_2 radiative balance in the IR is an important contribution to the thermal balance in the upper mesosphere/lower thermosphere [e.g., *Bougher and Dickinson*, 1988], so it is essential to account for it properly. At the low densities found above about 80 km in the Martian atmosphere the collisions are less frequent and Non-Local Thermodynamic Equilibrium (NLTE) prevails, which means that the kinetic temperature is not directly connected to the internal energy mode of the CO_2 molecules. Corrections to account for this situation had to be implemented.

2.1.1. NIR Heating Rate

[16] For the heating due to the absorption of NIR solar radiation by CO_2, the main impact of the NLTE is that a fraction of the energy absorbed is emitted back to space instead of heating the gas as in LTE. Detailed calculations of the solar heating rate using a full NLTE model performed by *López-Valverde et al.* [1998] show a weak dependence on the temperature and composition of the atmosphere. This allowed them to tabulate correction factors that convert LTE radiative transfer calculation heating rates into realistic NLTE heating rates.

[17] Using this tabulation, we have updated the method described in paper 1 to compute the NIR heating rate. At pressure $p_0 = 700$ Pa and for a mean Mars-to-Sun distance $r_0 = 1.52$ AU, the heating rate (per Martian day) corresponding to a zero solar zenith angle ($\mu = 0$) is taken to be

$$\frac{\partial T}{\partial t}(p_0, r_0, 0) = 1.1956\ \mathrm{K\ day^{-1}} \tag{1}$$

The heating rate at another pressure p, Mars-to-Sun distance r, and zenithal angle μ is then computed as follows:

$$\frac{\partial T}{\partial t}(p, r, \mu) = \frac{\partial T}{\partial t}(p_0, r_0, 0) \times \frac{r_0^2}{r^2} \sqrt{\frac{p_0}{p}}\,\tilde{\mu} \left(1 + \frac{p_1}{p}\right)^{-b} \tag{2}$$

with $p_1 = 0.0015889$ Pa, $b = 1.9628$ and $\tilde{\mu}$ the cosine of the solar zenith angle corrected for atmospheric refraction (we use $\tilde{\mu} = [(1224\mu^2 + 1)/1225)]^{1/2}$).

2.1.2. Thermal Cooling Rate

[18] The CO_2 15 μm cooling has a key role in the upper atmospheres of the terrestrial planets. The different balances between this process, the UV solar heating, the thermal conduction and the dynamical heating in the thermosphere of Mars, Earth and Venus explain, for example, the different responses to the solar cycle in the three thermospheres [*Bougher et al.*, 1999a].

[19] For the thermal cooling rate, calculations with a detailed 1-D model [*López-Puertas and López-Valverde*, 1995] show a strong dependence of the cooling rate with the thermal structure, preventing us from using an approach similar to the one described above. Instead, two main simplifications have been made to the full 1-D model to make it suitable for a GCM. First, the number of transitions between molecular levels is reduced to 2: the fundamental band of the main isotope, which produces most of the cooling in the upper atmosphere, and a "synthetic band" tuned to comprise the other transitions which significantly affect the cooling rate at lower altitudes. This is possible because all these weaker transitions share the same energy source, and therefore they can be treated jointly without being too unrealistic. The second simplification concerns the calculation of the radiative transfer, for which the "cool-to-space" approximation, using tabulated escape functions, is used.

[20] It is a well-known effect that the collisions with atomic oxygen excite the vibrational levels of the CO_2 molecule, enhancing its emission rate and thus the cooling (see, for example, the review by *Huestis et al.* [2008]). This effect is taken into account in this parameterization. However, although the GCM accounts for the variability of atomic oxygen (as well as of the other species) owing to the general circulation, the photochemistry and other processes, a fixed atomic oxygen concentration, independent of that predicted by the model, is used internally by this parameterization. The reasons and consequences of this assumption are discussed in the work by *Forget et al.* [2009]. The effects are expected to be higher in the regions with high atomic oxygen concentration (for example, the polar night), probably underestimating the cooling (i.e., overestimating the temperatures) there. Calculations utilizing an interactive, variable atomic oxygen concentration within this CO_2 cooling scheme do capture the winter polar warming features observed [e.g., *Bougher et al.*, 2006].

[21] In the lower layers, a more sophisticated LTE wide-band model is used [*Hourdin*, 1992; *Forget et al.*, 1999], so we merge the results from both models by

$$Q = \alpha Q_{\mathrm{NLTE}} + (1 - \alpha) Q_{\mathrm{LTE}} \tag{3}$$

with $\alpha = 1/(1+ (\frac{p}{p_{\mathrm{NLTE}}})^4)$ and $p_{\mathrm{NLTE}} = 0.1$ Pa the pressure level where the transition is centered.

2.2. UV Heating

[22] UV heating is the primary energy source of the terrestrial planets' upper atmospheres [*Hougton*, 1977], so an accurate simulation of this process is essential to obtaining a realistic thermal structure in this region.

[23] We use the parameterization presented by *González-Galindo et al.* [2005] to simulate the heating due to the absorption of solar UV radiation by CO_2, atomic oxygen

and a number of minor species. The UV visible spectral range (1–800 nm) is divided in 36 subintervals of varying spectral width. The photoabsorption coefficients integrated in each interval are calculated using a 1-D detailed model and tabulated as a function of the column amount. Using this tabulation, an interpolation to the actual column amount and a sum of the partial photoabsorption coefficients suffices to obtain the total photoabsorption coefficients for each species. From them, it is straightforward to obtain the UV heating rate.

[24] This strategy, which produces the photoabsorption coefficient with errors lower than 5% and an important CPU saving, has already been used in terrestrial models [*Zhao and Turco*, 1997; *Chipperfield*, 1999]. However, it has not been used before in Martian models. For example, the MTGCM uses an integration in discrete spectral intervals in which the cross sections are averaged [*Bougher et al.*, 1999a]. When using similar solar fluxes and cross sections, both methods give similar results [*González-Galindo et al.*, 2006].

[25] The variation of the UV solar flux with the 11-years solar cycle is taken into account by a sinusoidal fit, in each of the 36 subintervals, to the solar flux time curve during the solar cycles 22nd and 23rd given by the SOLAR2000 database [*Tobiska et al.*, 2000]. We do not use the $F_{10.7}$ index as a proxy for the solar flux, given that its correlation with the UV solar flux in narrow spectral subintervals is uncertain [*Donnelly et al.*, 1986]. However, this makes difficult the comparison with other models and with data, which are usually expressed as a function of this index. An intermediate approach, using a proxy index for the UV, the $E_{10.7}$ index, that can be related to the more commonly used $F_{10.7}$ index [*Tobiska*, 2001], is envisaged in the near future.

[26] A correction to account for the dependence on temperature of the CO_2 cross section, that some authors have shown to have a nonnegligible effect over the photoabsorption coefficients [*Nair et al.*,1994; *Anbar et al.*, 1993], is included assuming a linear dependence of the CO_2 cross section between 195 K and 295 K. No temperature dependence is considered out of this interval.

2.3. Thermal Conduction and Molecular Viscosity

[27] Thermal conduction is the dominant mechanism of cooling of the upper Martian atmosphere. In particular, it provides the primary cooling mechanism that balances the UV heating at its peak altitude [*Bougher et al.*, 1999a]. Molecular viscosity tends to smooth velocity gradients.

[28] Both processes are governed by similar equations. For the thermal conduction, the equation to solve is

$$\frac{\partial T}{\partial t} = \frac{1}{\rho c_p}\frac{\partial}{\partial z}\left(k\frac{\partial T}{\partial z}\right) \tag{4}$$

where T is the temperature (K), ρ the density (kg/m^3) and k the thermal conduction coefficient (J m^{-1} s^{-1} K^{-1}), expressed as $k = AT^{0.69}$, with A a number density weighted average of the individual thermal conductivities.

[29] For the molecular viscosity,

$$\frac{\partial S}{\partial t} = \frac{1}{\rho}\frac{\partial}{\partial z}\left(\mu\frac{\partial S}{\partial z}\right) \tag{5}$$

where S stands for the components of the horizontal wind (m s^{-1}) and μ is the coefficient of molecular viscosity (kg m^{-1} s^{-1}) that is related to the thermal conduction coefficient by $k = \frac{1}{4}[9c_p - 5(c_p - R)]\mu$. Given its similarity, both equations are discretized and solved using the same implicit numerical schemes, allowing for longer and more stable time stepping.

2.4. Molecular Diffusion

[30] The lower atmosphere is generally a well-mixed region, where the concentrations of the species do not present important changes with altitude. Note that the photochemistry and other processes, such as CO_2 condensation, can induce departures from this situation. In our model, the mixing is achieved by different processes. The general circulation is responsible of some of the mixing, and the turbulent mixing of chemical species at the subgrid scale is also taken into account from the turbulent kinetic energy diagnosed by the model in each grid box. In addition, a standard energy-conserving convective adjustment scheme rapidly mixes heat, momentum and tracers in convectively unstable layers. These parameterizations are described in detail in the work by *Forget et al.* [1999]. Above the homopause the species are no longer well mixed, as molecular diffusion dominates the vertical distribution of the different species. This allows each to progressively follow a vertical distribution given by their own scale height.

[31] We use in our model the exact theory of multicomponent diffusion, in which all the species are diffused simultaneously, following *Dickinson and Ridley* [1972]. They show that, after neglecting the thermal diffusion and nonlinear terms in the general equation of motion, the molecular diffusion equation can be written in matrix form as

$$\frac{\partial \psi}{\partial t} = \frac{\partial}{\partial z}\left[\frac{\bar{m}g^2}{pkT}\hat{\alpha}^{-1}L\psi\right] \tag{6}$$

where $\bar{m}$ is the mean molecular mass (kg mol^{-1}), g the gravity (m s^{-1}), p the pressure (Pa), k the gas constant, T the temperature (K), ψ a N−1 vector (where N is the total number of species) containing the mass mixing ratios of all the species except atomic oxygen, L is a N−1 × N−1 matrix operator with elements $L_{ij} = \delta_{ij}[\frac{\partial}{\partial z} - \epsilon_{ij}]$ and $\epsilon_{ij} = 1 - \frac{m_i}{\bar{m}} - \frac{1}{\bar{m}}\frac{\partial \bar{m}}{\partial z}$, $\hat{\alpha}$ is an N−1 × N−1 matrix with elements

$$\hat{\alpha}_{ij} = -\frac{1}{n}\left[\frac{1}{m_O D_{iO}} + \sum_{k\neq 1}^{N-1}\left(\frac{1}{m_k D_{ik}} - \frac{1}{m_O D_{iO}}\right)\psi_k\right] \quad j = i$$

$$\hat{\alpha}_{ij} = \frac{1}{n}\left(\frac{1}{m_j D_{ij}} - \frac{1}{m_O D_{iO}}\right)\psi_i \quad j \neq i$$

where n is the total number density (m^{-3}), D_{ij} stands for the coefficient of mutual diffusion between the species i and j (m^2 s^{-1}), m_j is the molecular mass of the species j (kg mol^{-1}) and D_{iO} and m_O are the coefficient of diffusion between the species i and atomic oxygen and the molecular mass of atomic oxygen, respectively.

[32] A special role is given to atomic oxygen. For this particular species, the changes of concentration produced by the molecular diffusion are not calculated using the procedure indicated above, but after calculating the other con-

centrations and using the simple relation $\sum_{i=1}^{N} \psi_i = 1$. We have chosen to do so with atomic oxygen, that is the major species in the upper atmosphere, but we could have done so for any other species. For example, in the works by *Dickinson and Ridley* [1972, 1975] in which a similar method is applied to the Venus thermosphere, this condition is applied to calculate the concentration of CO_2 that is not the major species in the upper thermosphere.

[33] The mutual diffusion coefficients are calculated following *Nair et al.* [1994]: the coefficients D_{ij}, which are supposed to be symmetric ($D_{ij} = D_{ji}$) are scaled to the coefficient of diffusion through molecular hydrogen by the square root of the ratio of molecular masses.

[34] After expansion and discretization using an implicit method of equation (6), a tridiagonal system of equations is obtained, with coefficients related to $\hat{\alpha}$ and ϵ.

[35] In the upper boundary, Jeans thermal escape [*Hunten*, 1973] is used for H and H_2 at the uppermost layer, while diffusive equilibrium is used for the other species. In particular, the concentration of each species at the upper layer of the model, $\psi_i(nz)$, is calculated by

$$\psi_i(nz) = \frac{\phi_i m_i}{\rho \omega_i} + \chi_i \cdot \frac{4\psi_i(nz-1) - \psi_i(nz-2)}{3 - 2\Delta p \cdot \epsilon_{ij}} \qquad (7)$$

where ϕ_i and ω_i are calculated according to *Hunten* [1973] for H and H_2 and ϕ_i is set to 0 for the other species, χ_i is 0 for H and H_2 and 1 for the other species, and $\Delta p = -\log(p(nz) - p(nz-1))$.

[36] In the lower boundary, perfect mixing of all the species is imposed. For that, the mixing ratios in the lowest layer are set equal to those in the layer just above. Note that this is only a numerical trick to calculate the profile of changes of concentration produced by the molecular diffusion. At the lower levels of the model the effects of the molecular diffusion are small, given the $1/\rho$ dependence of the molecular diffusion coefficients. Other processes, such as the photochemistry, produce changes of concentration that largely exceed those of the molecular diffusion at these levels, and can produce departures of this situation of perfect mixing.

[37] The tridiagonal system is solved using standard numerical methods, and the variations of concentration due to molecular diffusion for all the species are obtained. Although this method is fast enough to be used in a GCM, the inversion of the $N-1 \times N-1$ matrix α increases significantly the CPU time consumed when the number of species N is large. This is not a serious limitation for this version of the GCM with 13 chemical species undergoing molecular diffusion, but it will be important to take this limitation into account if future versions of the model are to include more species.

[38] The method in which this molecular diffusion scheme is based, summarized in the work by *Dickinson and Ridley* [1972, 1975] is also at the base of the scheme used in the NCAR family of models, including the MTGCM. More sophisticated schemes, but less suitable for GCMs, have been developed [e.g., *García Muñoz*, 2007].

2.5. Photochemistry of the Upper Atmosphere

[39] A photochemical model specifically developed for the low densities of the Martian upper atmosphere is used in our GCM, based on *González-Galindo et al.* [2005]. The model considers 12 constituents in the C, O and H families (in particular, CO_2, CO, O_3, O_2, O, $O(^1D)$, H, OH, HO_2, H_2, H_2O, H_2O_2,) and 27 reactions between them, including photodissociations. Although it is designed for the simpler chemistry of the Martian upper atmosphere, the most important catalytic cycles to recover CO_2 are included. These cycles are important for the long-term stability of the Martian atmosphere and happen mainly in the lower atmosphere. However, this model is used in the GCM only for altitudes above about 80 km. Below, the photochemical model described by *Lefevre et al.* [2004] is used, since it includes all the reactions that are important in the more dense lower atmosphere. Some of these reactions are not included in our model, as they are not important in the upper atmosphere and their inclusion would negatively affect the CPU time consumption, without modifying the results. Some tests have been conducted that show that in the 60–100 km region, where both models overlap, their results are similar.

[40] The reaction rates are taken from the latest JPL compilation [*Sander et al.*, 2006], although modifications to some rates, within their error range, proposed by *Nair et al.* [1994], have been maintained. The photodissociation rates are calculated from the photoabsorption rates provided by the tabulation described above for the UV heating, using dissociation-to-ionization branching ratios.

[41] The approximation of photochemical equilibrium for $O(^1D)$, OH and HO_2 (the species with shortest lifetimes) is used to avoid an excessive CPU time consumption, as the time step used by this photochemical model is given by the shortest lifetime of the species. For the other species, the time marching is solved using an implicit method to avoid further limitations to the time step.

[42] It has to be noted that, up to now, the model only considers neutral species. However, it is known that some reactions with ions can impact the neutral concentrations. A brief discussion on this impact on the results can be found in the work by *González-Galindo et al.* [2005]. Given that this is a current limitation of our model and the recent observations of the Martian ionosphere [*Bougher et al.*, 2004; *Pätzold et al.*, 2005], we are currently working on the development of an ionospheric model to be included in the GCM [*Gilli et al.*, 2007].

2.6. Vertical Coordinates

[43] The model described in paper 1 used $\sigma = p/p_s$ terrain following coordinates, which allowed for a constant domain, but made the topography visible up to the top of the model. To avoid this effect, the new version of the LMD-MGCM uses hybrid coordinates, i.e., σ levels in the near surface and lower atmosphere and pressure levels in the upper layers, with a soft transition between them. With this representation, the pressure at a given layer l is given by $P(l) = a(l) + b(l) \times P_s$. In the lower layers, $a(l) = 0$ and $b(l) = P/P_s$, corresponding to σ coordinates. Above about 50 km, $b(l) = 0$ leading to pressure levels.

[44] When including the thermosphere, 50 vertical layers are used, with an uneven sampling to allow for a higher vertical resolution in the lower layers. For reference, we list here the pressure of the 30 upper layers, in Pa: 0.44, 0.22, 0.11, 5.4×10^{-2}, 2.7×10^{-2}, 1.3×10^{-2}, 6.7×10^{-3},

3.3×10^{-3}, 1.6×10^{-3}, 8.2×10^{-4}, 4.0×10^{-4}, 2.0×10^{-4}, 1.0×10^{-4}, 4.9×10^{-5}, 2.5×10^{-5}, 1.2×10^{-5}, 6.1×10^{-6}, 3.0×10^{-6}, 1.5×10^{-6}, 7.4×10^{-7}, 3.7×10^{-7}, 1.8×10^{-7}, 9.1×10^{-8}, 4.5×10^{-8}, 2.2×10^{-8}, 1.1×10^{-8}, 5.5×10^{-9}, 2.8×10^{-9}, 1.4×10^{-9}, 6.8×10^{-10}. This vertical distribution corresponds to a vertical spacing of about 7 km in the upper atmosphere.

3. Input Data

[45] As commented above, *Bell et al.* [2007] have shown that the dust load of the lower atmosphere can have an important influence over the temperatures in the lower thermosphere (about 130 km). So, if realistic results want to be obtained, an appropriate dust scenario has to be used. For the simulations presented here, we use a climatology of the dust as observed by TES on board MGS between 1999 and June 2001 (Mars Year 24, following *Clancy et al.* [2000] nomenclature), a Martian year thought to be typical [*Smith*, 2004]. For its vertical distribution, we use an approach similar to the one by *Montmessin et al.* [2004]. Basically, the dust mass mixing ratio q at a pressure level p is given by

$$q = q_0 \cdot \exp\left(v(1 - p/p_0)^{(70/z_{\max})}\right) \tag{8}$$

where q_0 is a constant determined by the prescribed opacity at a reference pressure level p_0 ($\approx$7 mbar), v is the so-called Conrath parameter, that in out simulation is fixed at a value of 0.007, and $z_{\max}$ (km) is taken from *Montmessin et al.* [2004]. For pressure levels higher than p_0, q is set equal to q_0.

[46] There are two key parameters for the thermal balance in the upper atmosphere: the UV heating efficiency and the O-CO_2 deactivation rate. The first one represents the fraction of UV energy absorbed that is finally thermalized. The second one governs the efficiency of excitation of CO_2 vibrational levels by collisions with atomic oxygen. It determines, together with the relative abundance of O atoms, the magnitude of the 15 μm cooling.

[47] For the UV heating efficiency, calculations by *Fox et al.* [1996] yield standard efficiencies between 19 and 23% for Mars, while their extreme "lower-limit" model gives values between 16 and 20%. The value of the O-CO_2 deactivation coefficient has been a subject of discussion during 2 decades. While the measurements seem to indicate a room temperature value around 1.5×10^{-12} cm^3 s^{-1} (although additional low-temperature measurements may be needed), GCMs generally use a higher value of about 3×10^{-12} cm^3 s^{-1} to reproduce the observed temperatures in the upper atmosphere. This discrepancy is probably due to the uncertainties in the atomic oxygen abundances in the upper atmosphere [*Huestis et al.*, 2008].

[48] In this paper we use a 16% heating efficiency, lower than the recommended value (but still into the "lower-limit" model developed by *Fox et al.* [1996]) and the traditional value of 3×10^{-12} cm^3 s^{-1} for the O-CO_2 deactivation rate. The reason is that early comparisons with measured exospheric temperatures showed that the model overestimated the temperatures if a 21% heating efficiency or a lower value for the O-CO_2 deactivation rate were used [*González-Galindo*, 2006]. This is probably due to the fixed atomic oxygen concentration used internally in the 15 μm parameterization, that as explained above may produce an underestimation of the CO_2 cooling. The development of an improved CO_2 cooling scheme that will incorporate the atomic oxygen concentration predicted by the model [*López-Valverde and González-Galindo*, 2008], will allow us to revisit this discussion in the future and to use more standard values for these coefficients.

[49] If not indicated, a solar flux appropriate for solar average conditions is used. Variations with the 11-year solar cycle will be studied in section 6. For that study, the solar flux is varied according to the scheme presented by *González-Galindo et al.* [2005].

4. Seasonal Variability of Temperatures

4.1. Temperatures at the Exobase

[50] Using the input data specified in section 3, we have performed a simulation during 1.5 Martian years. The first half a year is used as a spin-up period, and we analyze the results for the remaining Martian year. We would like to remark that, to our knowledge, this is the first time that a Martian GCM covering the thermospheric altitudes has continuously simulated a full Martian year. Previous thermospheric works [e.g., *Bougher et al.*, 2000; *Bell et al.*, 2007] showed results of GCMs integrated for relatively short periods of time (typically 10 days) at different orbital conditions. This strategy allowed them to study aspects such as the seasonal variation of temperatures, but we think that the analysis of a simulation of a full Martian year will no doubt add interesting information to the previous valuable knowledge built upon those shorter integrations.

4.1.1. Seasonal Variations

[51] Figure 1 shows the latitudinal and seasonal variation of the zonal mean temperatures for solar moderate conditions at a constant pressure surface of 10^{-6} Pa (approximately 200 km), well above the 160 km value for the exobase given in the work by *Hunten* [2002]. As we will see later, this layer is high enough to be in the thermospheric region where the temperatures do not change with altitude. Following *Hunten* [2002], the exobase is located approximately at the lower limit of this isothermal region, so the temperatures at the 10^{-6} Pa layer should be equal to the temperatures at the exobase. We can then consider the temperatures that will be presented in this work as exobase (or exospheric) temperatures. A smoothing over 10 time steps (5 h) has been applied to minimize the short-time variations and to allow for a better visualization of the seasonal variation. Obviously, the zonal average mixes day and nighttime information. In the lower atmosphere, the day-night differences are generally small when compared with the vertical and latitudinal variations of temperature, and a zonal mean can be very representative of the average atmospheric conditions. However, this is not the case in the upper atmosphere, especially in the thermosphere, where the absorption of UV solar radiation imposes a strong day-night cycle, as we will see later. It is important to have this in mind when using zonal means in the upper atmosphere.

[52] As expected, there is a strong seasonal variation of the temperatures, shown in Figure 1. Temperatures are minimum during the aphelion season (around L_s = 70)

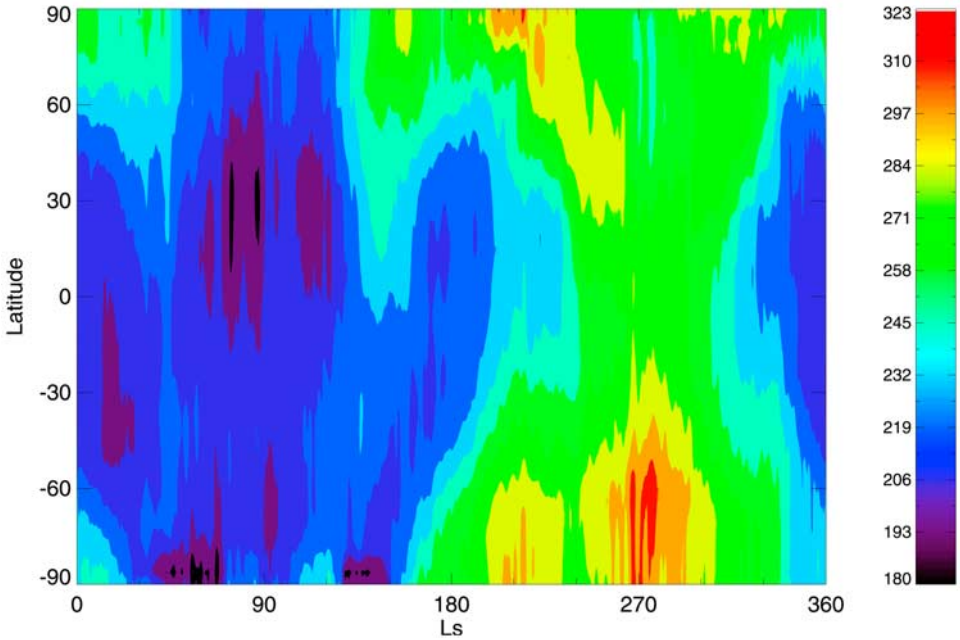


Figure 1. Seasonal variation of zonal mean temperatures (K) at the exobase level (P $\approx 10^{-6}$ Pa) for solar average conditions.

and maximum around the perihelion season (about L_s = 250). The seasonal variation of the temperature has an approximate magnitude of 90 K (from around 195 K during aphelion to 285 K at perihelion) in the equatorial regions. It reaches about 120 K (from approximately 195 K to 315 K) in the south polar region. As an illustration of the day and night mixing described above, we note that these values change if we consider, instead of a zonal average, a day mean average (0600–1400 Local Time (LT)) or a night mean (1400–0600 LT) average. In these cases, the seasonal variation at the equator is about 100 K (from 210 to 310 K) for the day mean temperatures, and of about 75 K (from 180 to 255 K) for the night mean temperatures.

[53] This seasonal variation is higher than the ≈50 K variation for the exobase equatorial temperatures at 1500 LT reported for a dust-free lower atmosphere by *Bougher et al.* [2000] using the MTGCM. However, when forced by similar input conditions (i.e., similar UV solar fluxes and similar dust load), both models predict similar mean temperatures at L_s = 90 and L_s = 270 [*González-Galindo et al.*, 2006], so those differences can be attributed to differences in the input conditions.

[54] The seasonal cycle is more intense in the thermosphere than in the lower atmosphere. For example, at 50 Pa, our model predicts temperatures varying between ≈160 K at aphelion and ≈200 K at perihelion, in very good agreement with the temperatures observed at this pressure level by TES [*Smith*, 2004].

[55] The seasonal variation of thermospheric temperatures has different components: it can be due to the variation of the Sun-Mars distance and the solar declination, and the variability of the dust content in the lower atmosphere, which could affect the dynamics of the upper atmosphere. Given the difficulty to distinguish these effects in the current simulation, another annual integration of the GCM, using a dust-free lower atmosphere, has been performed. Although the temperatures in the lowest layers of the atmosphere are significantly reduced with respect to the nominal simulation, the change of temperatures in the thermosphere (above about 10^{-3} Pa), represented in Figure 2, is generally lower than 15 K, with maximum differences of about 30 K in the polar night during solstices. This is a small effect when compared with a seasonal evolution of about 100 K.

[56] We can thus conclude that the seasonal variability of the thermospheric temperatures presented in Figure 1 is dominated by the Sun-Mars distance, with the seasonal variability of the dust load producing only small modifications. A similar conclusion was found in the work by *Forbes et al.* [2008], who studied the seasonal variation of the exospheric temperatures by MGS drag measured using Precise Orbit Determination. They found that the variations in the dust content of the lower atmosphere did not significantly affect the exospheric densities and temperatures. Note that this does not necessarily imply that a stronger modification in the dust distribution, such as the ones typical of a global dust storm, will not affect the temperatures in the thermosphere.

[57] It also has to be remarked that this conclusion does not imply that the dust does not affect the thermospheric temperatures. For example, *Bell et al.* [2007] have shown that changes in the dust distribution affect the magnitude of the polar warming in the lower thermosphere. This is not in contradiction with our results, since a ≈15 K difference in temperature, small when compared with the amplitude of the seasonal cycle, can be important for other phenomena, such as the thermospheric polar warming, with a typical magnitude of ≈40 K. Furthermore, during the solstices, the biggest effect of using a dust-free lower atmosphere is felt at the polar night region, whereas the low and middle latitude regions are less affected. As a consequence, the latitudinal distribution of the temperatures is modified, changing the intensity of the thermospheric polar warming.

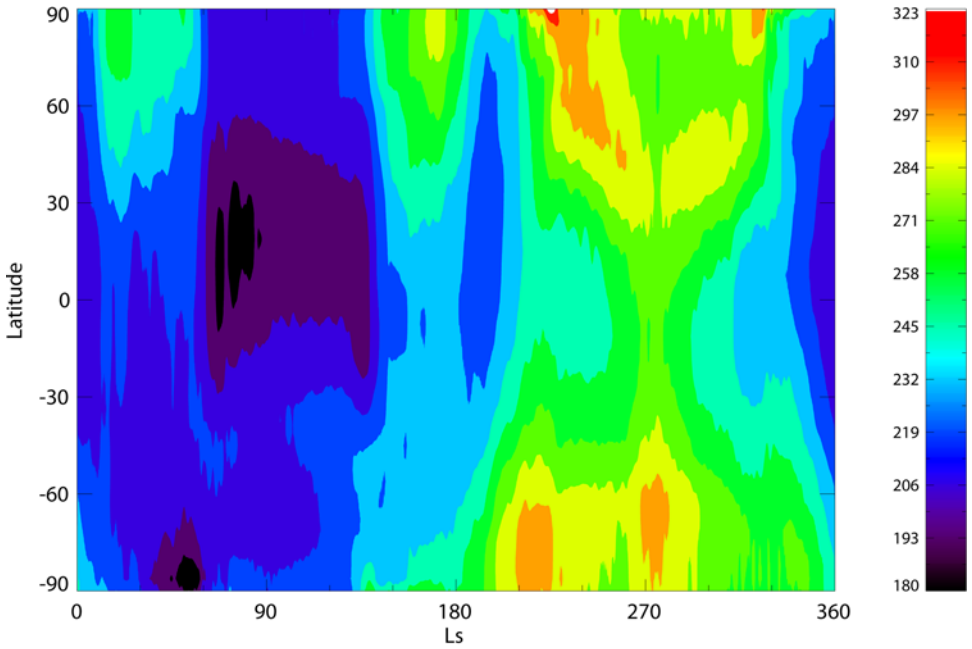


Figure 2. Seasonal variation of zonal mean temperatures (K) at the exobase level (P $\approx 10^{-6}$ Pa) for a simulation with a dust-free lower atmosphere solar average conditions.

4.1.2. Latitudinal Variations

[58] A detailed analysis of Figure 1 allows us to study the latitudinal variation of the zonal mean temperatures for a fixed season. Around the equinoxes (L_s = 0,180) temperatures are higher in the high-latitude regions than in middle and low latitudes. This reflects the fact that, during equinoxes at these altitudes, the polar regions are constantly illuminated, and the zonal mean UV heating is higher there (figure not shown). An adiabatic warming in the polar regions has a smaller but nonnegligible contribution to the high polar temperatures. For the northern summer solstice (L_s = 90) minimum temperatures of around 180 K are found around 30N latitude. The latitudinal variation of the temperatures is rather small, and in agreement with the temperature obtained during the aerobraking of MGS, which increased by about 25 K when MGS orbit periapsis moved from 30N to 30S at an altitude of 150 km during this season [*Keating et al.*, 2007; *Bougher et al.*, 2006]. For the southern summer solstice (L_s = 270), Figure 1 shows that the maximum zonal mean temperature (around 320 K) is found at high southern latitudes, with a latitudinal variation of temperature of around 90 K.

[59] As stated previously, the thermal state of the Martian thermosphere is determined mainly by the balance between the UV heating, the thermal conduction, the dynamical heating and the 15 μm cooling [e.g., *Bougher et al.*, 1999a]. The UV energy deposited in the high layers is efficiently conducted to lower layers, where it can be radiated away to space by CO_2. Given this efficient conduction, the exobase temperature is not entirely controlled by the in situ heating, but by the column integrated heating/cooling above the mesopause [*Strobel*, 2002]. Other factors, like the dynamics in the lower thermosphere, have an influence on the precise latitude-longitude distribution of the exobase temperature [*Bougher et al.*, 1999a, 2000; *González-Galindo*, 2006].

4.1.3. Diurnal Variations

[60] As stated before, a zonal average combines daytime and nighttime data and suppresses the longitudinal variation. Further insight can be gained into the seasonal behavior of the thermosphere by analyzing longitude-latitude maps at a given pressure level. We have divided the simulated Martian year into 12 ''months'', or temporal intervals of 30 units of L_s. In each of them, the results are averaged conserving the diurnal variation. For that, we take ''snapshots'' every day at given Universal Times, we average the results separately for each of the chosen UT, and merge these averages into a single file, so that a ''typical day'' is obtained for every month. In this way, the effect of thermal tides is included while removing the transient day-to-day variability, that we will examine below. We will show results for UT = 12.

[61] Figure 3 shows the evolution of the longitude-latitude distribution of temperatures at a constant pressure level close to the exobase (pressure around 10^{-6} Pa). Note that the longitude axis is equivalent to a local time axis, with noon at lon = 0. Maximum temperatures are usually obtained close to the evening terminator and minimum temperatures around midnight. A lot of small scale structure is observed, but its physical meaning is difficult to assess. So, we will focus mainly on the large-scale features.

[62] The shape of the temperature distribution changes according to the evolving solar illumination. The strong day-night variation of the temperatures is evident, and dominates over the latitudinal variations. We will focus on this day-night variation in section 5.

[63] Significant departures from the temperature distribution that would be expected by radiative equilibrium are obtained. There are cold areas during the day (for example, in low and middle latitudes during the first half of the day for L_s = 0–30 or for high southern latitudes at longitude around 60E for L_s = 240–270), generally associated with

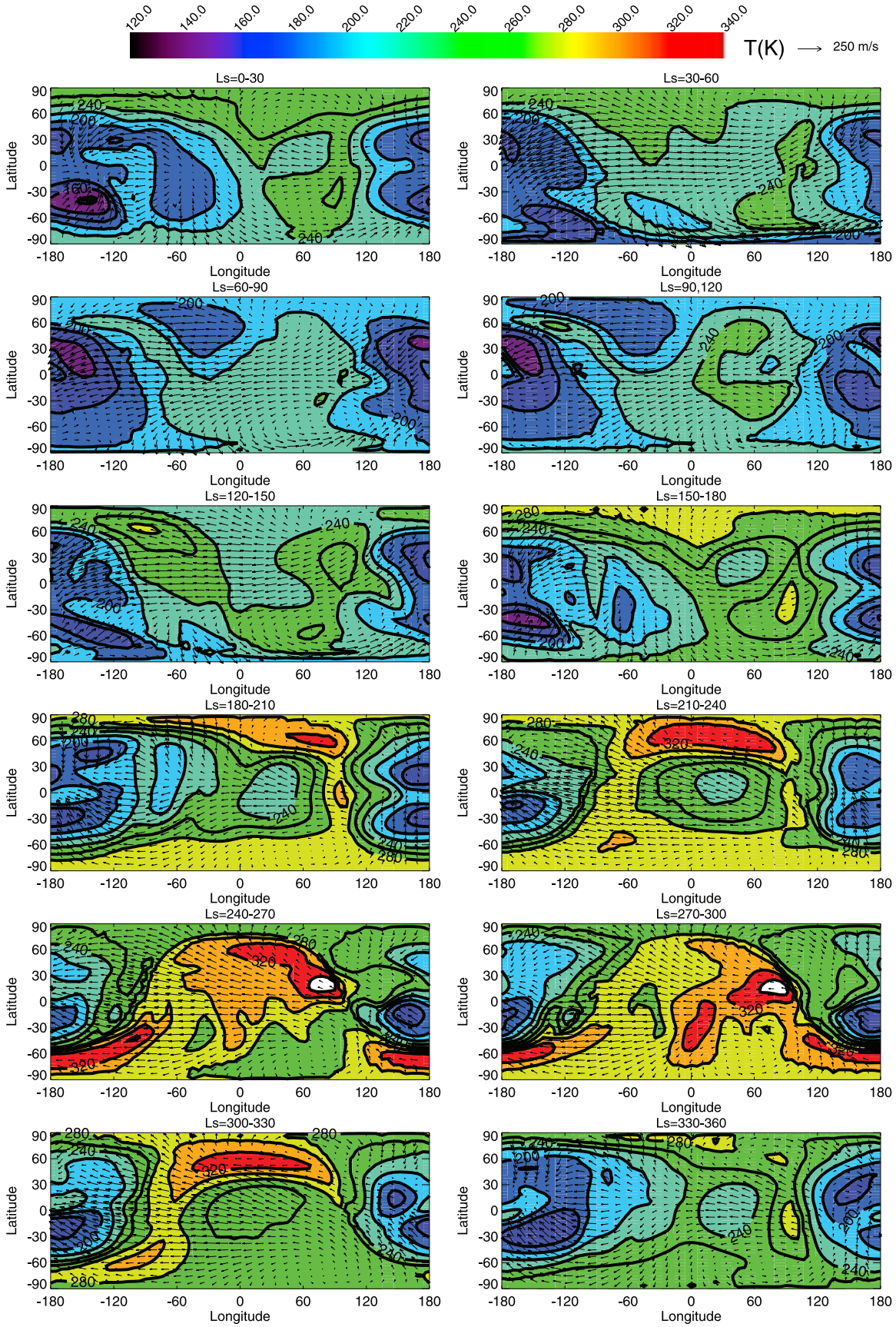


Figure 3. Average temperatures (K) at 1200 UT at the exobase level (P $\approx 10^{-6}$ Pa) for each "Martian month". Solar average conditions.

divergence of winds, and hot areas during the night and close to the terminators, where winds converge. This is the signature of a strong modification of the temperature distribution due to the dynamics, as previously described by *Bougher et al.* [1999a]. Similar features, affecting approximately the same regions, are obtained with the MTGCM [*González-Galindo et al.*, 2006].

[64] A good example of this effect of dynamics over the temperatures is the thermospheric polar warming. As commented above, it is attributed to a strong interhemispheric circulation from the summer hemisphere to the winter one [*Bougher et al.*, 2006]. Such a thermospheric polar warming is simulated with our model for both solstices seasons. For southern winter (seasons L_s = 60–90 and 90–120) this warming is rather modest (20–30 K during the night, similar to SPICAM observations in the lower thermosphere [*Forget et al.*, 2009]), while for northern winter (seasons L_s = 240–270 and 270–300) it is more intense (up to 60–70 K in the night side), in good qualitative agreement with the observations by Mars Odyssey, MGS and MRO, and the MTGCM simulations [*Bell et al.*, 2007]. This indicates, as pointed out by *Bougher et al.* [2006], a more intense intermeridional circulation during perihelion. We discuss this thermospheric polar warming in detail in a companion paper.

4.2. Vertical Structure of the Zonal Mean Temperatures: Mesopause

[65] Until now, we have focused on the thermal structure of a constant pressure layer in the upper thermosphere. But one of the lessons of the information obtained in the last years about this region is that it is strongly linked to what happens below [e.g., *Bougher et al.*, 2006; *Bell et al.*, 2007]. So, it is important to study the upper atmosphere in connection to the structure of the lower layers.

[66] All the plots that follow have been made using pressure as a vertical coordinate. However, an altitude scale has been added. Please note that this is only an approximate altitude, useful as a reference, but should not be considered an absolute altitude.

[67] The seasonal variation of the zonal mean temperature, from the troposphere to the upper thermosphere, is presented in Figure 4 for the 12 "months" of the simulation. As in Figure 1, the zonal average mixes the day and night hemisphere.

[68] The vertical structure is characterized, in all cases and as expected, by a decrease of temperatures with altitude in the low and middle atmosphere up to the minimum of temperature of the mesopause (indicated as a white line). Above this level, temperature increases with altitude in the lower thermosphere, tending asymptotically to a constant value in the upper thermosphere. In particular, the temperatures remain almost constant above 10^{-6} Pa, the pressure level chosen for representation in Figures 1 and 3, indicating that the temperatures shown there can be considered as exospheric temperatures.

[69] The results obtained in the low and middle atmosphere closely resemble those by *Forget et al.* [1999] for L_s = 270–300 and L_s = 90–120. In particular, a polar warming in the middle atmosphere similar to the one described by *Forget et al.* [1999] is obtained. This indicates that the overall thermal structure of the troposphere and the mesosphere is not strongly affected by the inclusion of the thermosphere in the simulations.

[70] The thermospheric polar warming is clearly visible at the solstices, especially at the mesopause/lower thermosphere levels at L_s = 240–270 and L_s = 270–300. More details about this thermospheric polar warming are given in a companion paper.

[71] The mesopause region has traditionally eluded direct observation. Only with the arrival of SPICAM on board Mars Express have we started to gather systematic data about this region. However, the mesopause is a very important region that can provide specific information about the energetic processes in the whole upper atmosphere. On an average basis, the mesopause is determined by the radiative balance [*States and Gardner*, 2000]. The location of the mesopause occurs, on average, at the altitude where the entire downward heat conduction flux (due to the integrated UV heating in the thermosphere) is radiated away in the IR [*Strobel*, 2002]. However, important departures from this average mesopause are driven by other processes, like chemical heating and propagation of waves and tides from below [*States and Gardner*, 2000].

[72] The mesopause level as obtained with the LMD-MGCM is shown as a white line in Figure 4. It is usually located between 0.1 and 10^{-3} Pa, and is characterized by a weak seasonal variation of the temperature. In the equatorial region the temperature of the mesopause varies between 116 and 130 K with no clear seasonal trend. Such a small seasonal variation is also found on Earth [*States and Gardner*, 2000] and is in good agreement with the 10–20 K seasonal variations at the mesopause measured by SPICAM at middle-low latitudes [*Forget et al.*, 2009]. Near the poles this variation is more important, between about 100 and 150 K. Over the entire planet, an analysis of day mean and night mean similar plots (figure not shown) shows that the temperature of the mesopause is only very weakly affected by the day-night cycle.

[73] The seasonal variation of the pressure level of the mesopause at 1400 LT and 0200 LT at two particular latitudes, representative of the situation at low and middle latitudes and high latitudes, is presented in Figure 5. At midlatitudes, the pressure level of the mesopause is stable, with little seasonal variations. The nightside mesopause is systematically placed at higher pressure (i.e., lower in the atmosphere) than the dayside mesopause. At high latitudes the day-night variation of the mesopause level is strongly reduced with respect to midlatitudes. During the polar winter, the mesopause is located at higher pressures than in the polar summer. This behavior is consistent with the theoretical expectations based on a radiative balance reasoning: during the day, the UV heating injects energy into the thermosphere, raising the level of the mesopause. During the night and the polar night, the UV heating is absent, and the continuous action of thermal conduction cools the upper atmosphere and lowers the level of the mesopause.

[74] SPICAM observations show a nighttime mesopause located between 10^{-3} and 10^{-4} Pa, with temperatures that can go below 100 K, well below the CO_2 condensation point [*Forget et al.*, 2009]. Our simulated mesopause is hotter, with temperatures generally above 110 K, and placed at lower layers than the one inferred from SPICAM thermal

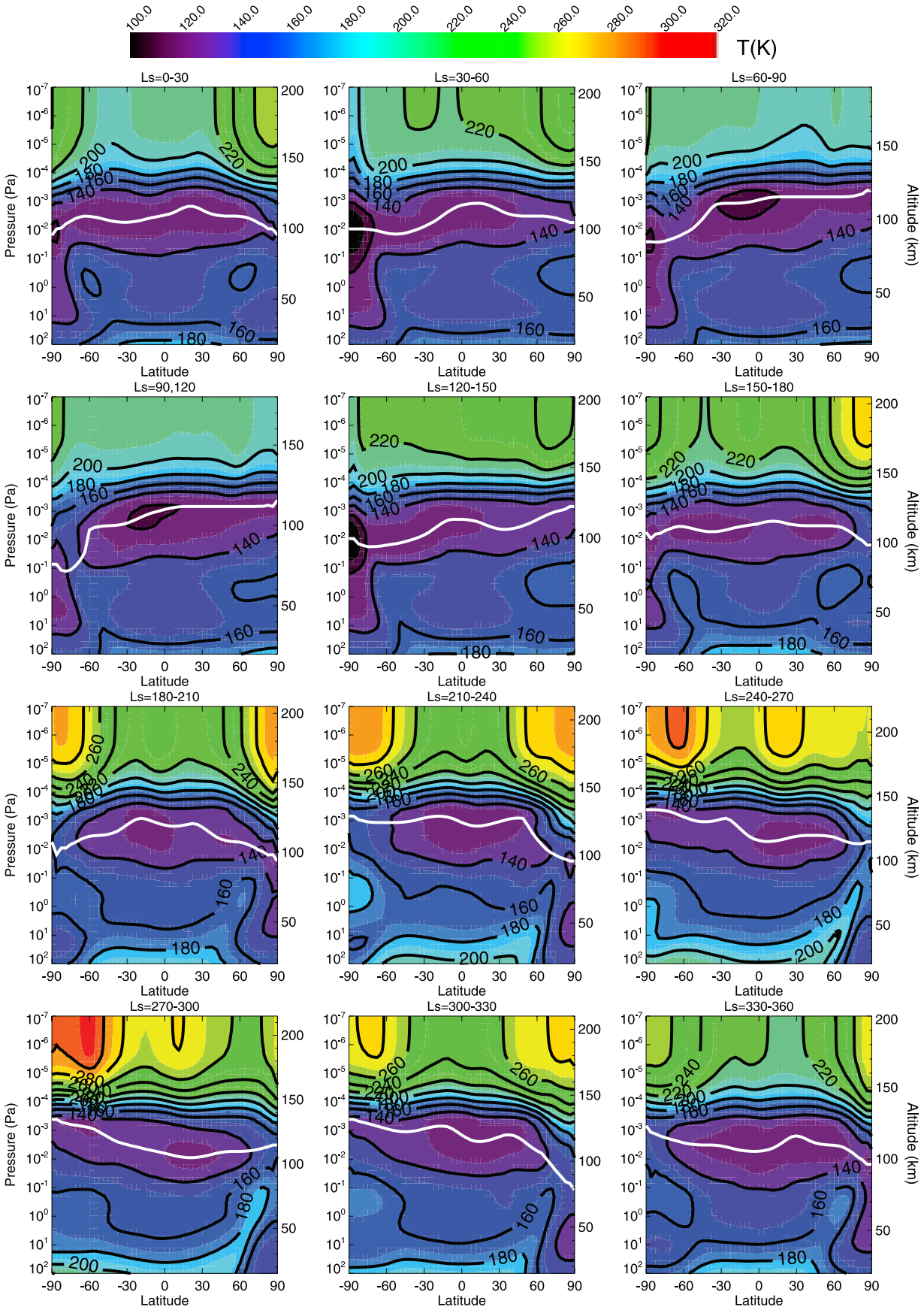


Figure 4. Zonal mean temperature profiles (K) for each Martian month. The white line illustrates the location of the mesopause.

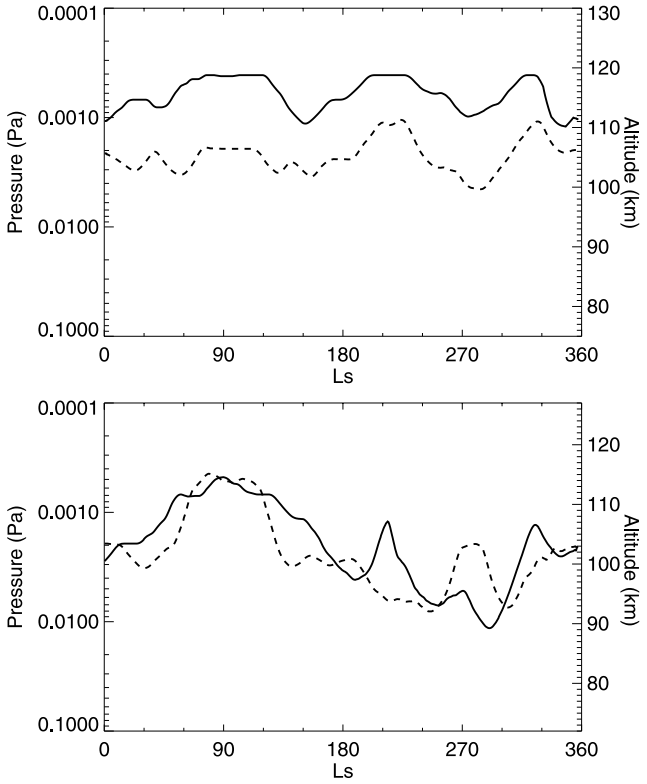


Figure 5. Pressure level of the mesopause at (top) 30°N latitude and (bottom) 70°N lat for 1400 local time (LT) (solid lines) and 0200 LT (dashed lines).

profiles. A possible explanation for this discrepancy is the simulation of the 15 μm cooling in our model, and specifically the role of atomic oxygen. More details can be seen in the work by *Forget et al.* [2009].

4.3. Vertical Variation of Mixing Ratios: Homopause

[75] Although this work is mainly focused on the temperature, other valuable insights can be obtained from the model. We are interested here in studying the vertical variation of the mixing ratios of the different species.

[76] According to this variation, the atmosphere has been traditionally divided in two regions. In the low atmosphere, the mixing produced by the general circulation and by turbulent and convective processes dominates over the molecular diffusion (which is inversely proportional to density). In this region, known as the homosphere, the diffusive separation is inhibited and the relative concentrations do not change strongly with altitude, although species subject to photochemistry can show departures of this idealized situation. In the rarefied upper atmosphere, where the densities are so low, the molecular diffusion has a dominant role and the vertical distribution of each species changes progressively with altitude according to its molecular mass. This region is known as heterosphere. The transition between these two regions is known as homopause, or also turbopause. In this section, we examine the pressure level at which the homopause is located.

[77] The vertical variation of the time and zonal mean mixing ratios of some selected species at the equator for two different "months", given by the LMD-MGCM, can be seen in Figure 6. In both cases, below a certain altitude ($\approx 10^{-3}$ Pa), the mixing ratios do not vary considerably with altitude. Above, the relative concentrations undergo important variations: the mixing ratio of CO_2, due to its high molecular mass, decreases with altitude, whereas the relative concentrations of lighter species, such as atomic oxygen, increase with altitude. Atomic oxygen, in particular, becomes more abundant than CO_2 at a certain altitude, different for each "month".

[78] Given the diffuse nature of this transition region, it is difficult to assign a precise altitude to the homopause. The observation of typical concentration profiles, such as those shown in Figure 6, shows that a good indicator of the transition between the homosphere and the heterosphere is the decrease in the CO_2 mixing ratio with altitude. For this reason, we have defined the homopause as the layer where the mixing ratio of CO_2 is 0.9. As we did with the mesopause, we can study the seasonal variations of the altitude of this layer at different latitudes. Note that, because of using for this study time mean values for the mixing ratios, we have only one value for the altitude of the homopause per month. However, a more detailed study using daily varying magnitudes gives similar results regarding the seasonal and latitudinal variations. Note also that, although the absolute value of the pressure level of the homopause will be strongly dependent on the convention

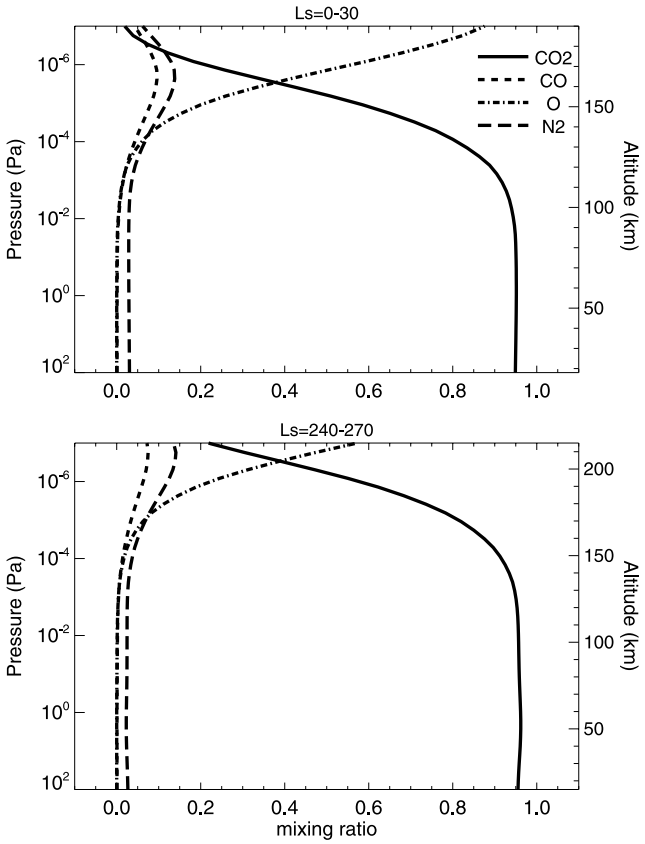


Figure 6. Time and zonal mean mixing ratio of CO_2 (solid line), CO (dashed line), O (dash-dotted line) and N_2 (long-dashed line) for (top) L_s = 0–30 and (bottom) L_s = 240–270.

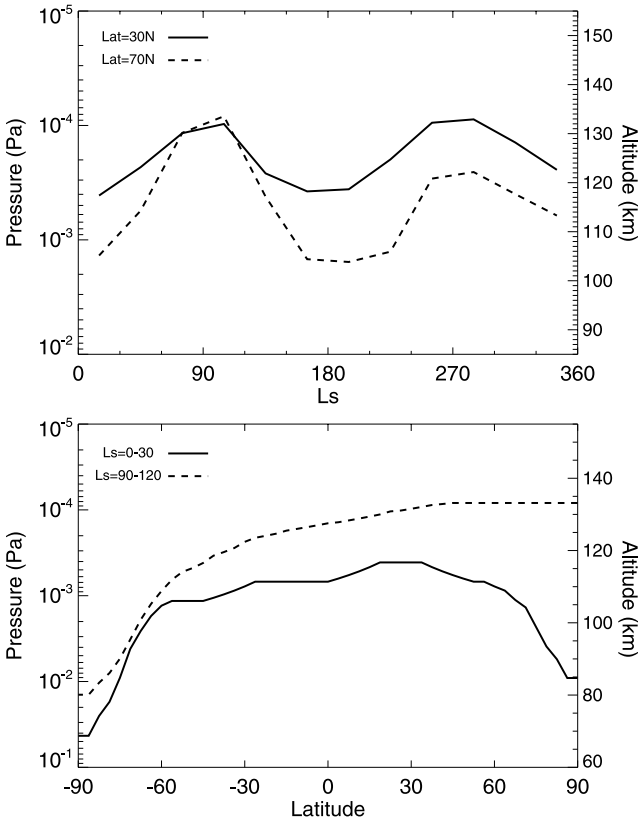


Figure 7. (top) Seasonal variation of the pressure level of the homopause at two fixed latitudes: 30°N (solid line) and 70°N (dashed line). (bottom) Latitudinal variation of the pressure level of the homopause at two particular seasons: L_s = 0–30 (solid lines) and L_s = 90–120 (dashed lines).

used to define it, its seasonal and latitudinal relative variations should not be strongly affected by this selection.

[79] The seasonal variation of the pressure level of the homopause is shown in Figure 7 (top) for two different latitudes. There is a clear seasonal evolution, with the homopause placed lower in the atmosphere during the equinoxes that during the solstices. This is the case not only for these two particular latitudes: LMD-MGCM results show this behavior for all latitudes. This result is indicative of a more intense mixing in the lower atmosphere owing to a reinforced general circulation during the solstice seasons. This behavior can also be seen in Figure 7 (bottom), where we show the latitudinal variation of the pressure level of the homopause for two different "months". As before, we can see, at all latitudes, the lower level of the homopause during the equinox season.

[80] It is also evident in Figure 7 (bottom) that the homopause is located at a lower level during the polar winter. This is indicative of a relative depletion of CO_2 in the upper atmosphere during the polar winter. Two different processes can be at the root of this depletion. First, it is well known that the cold temperatures at this season produce the condensation of CO_2 and a relative enrichment of non-condensible gases. And second, the general circulation can produce a downward transport of heterospheric CO_2-poor air from the midlatitudes upper thermosphere. This is the same circulation that generates the thermospheric polar warming. The results of our model show (figure not shown) that the effect of the condensation of CO_2 is only felt in the lower layers, below about 10–20 km, indicating that this depletion of CO_2 (and enhancement of O) in the polar winter upper atmosphere is mainly due to transport of air from the midlatitudes upper thermosphere.

[81] The atomic oxygen concentration in the lower thermosphere is an important parameter for the thermal balance, as it affects the 15 μm cooling, but unfortunately observations are scarce. Using Mariner 9 airglow observations,

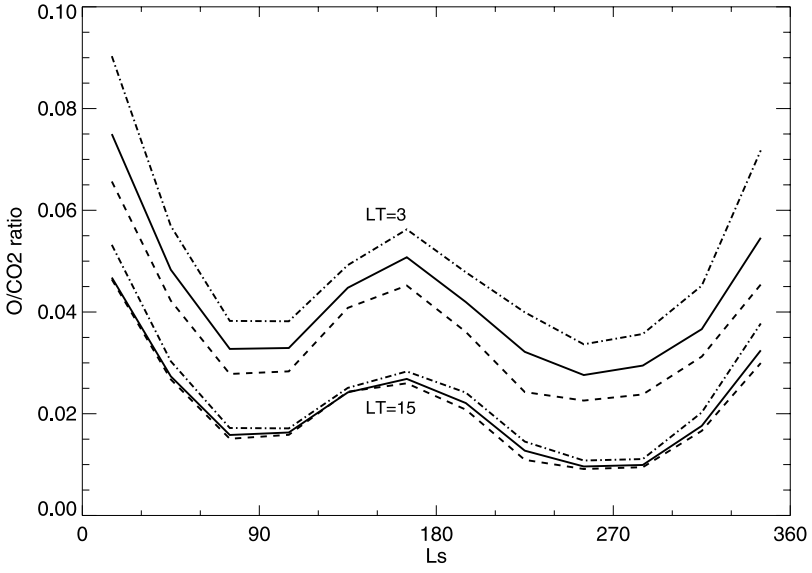


Figure 8. Relative abundance of atomic oxygen at the 1.4×10^{-4} Pa constant pressure level at 1500 LT and 0300 LT for solar maximum (dash-dotted line), average (solid line), and minimum (dashed line) conditions.

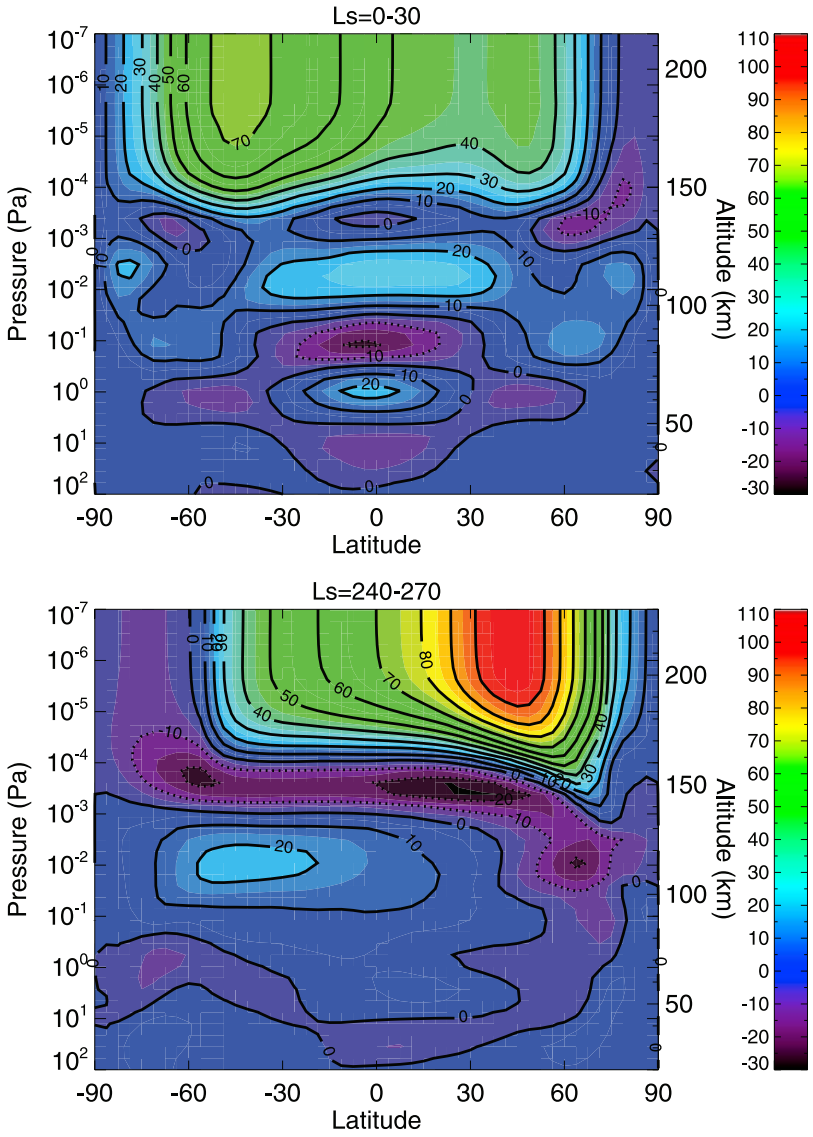


Figure 9. Day-night (1400 LT−0200 LT) difference of temperature for (top) L_s = 0−30 and (bottom) L_s = 240−270.

Stewart et al. [1992] inferred atomic oxygen abundances, varying between 0.4% and 1% at the 1.2 nbar level for L_s = 290−350. The longitude averaged O/CO_2 ratio predicted by the model at a constant pressure level of 1.4×10^{-4} Pa is shown in Figure 8 for 1500 LT and 0300 LT and for different solar conditions. During daytime the O/CO_2 ratio is found to vary between 1 and 5%. At L_s = 300, corresponding approximately to the season of observation of Mariner 9, the abundance of atomic oxygen at 1500 LT is of about 1−1.5%, slightly higher than the observed value. The atomic oxygen is efficiently transported from the dayside thermosphere, where it is produced by photodissociation, to the nightside. As a consequence, the nightside thermosphere shows a higher O/CO_2 ratio, between about 2.5 and 9%. Similar values were obtained with the MTGCM [*Bougher et al.*, 1999a, 2000].

[82] The seasonal evolution of the O/CO_2 ratio is well correlated with that of the altitude of the homopause, as can be seen by comparison of Figure 8 with Figure 7 (top). The atomic oxygen relative abundance at the 1.4 nbar level is higher during the seasons where the homopause is lower in the atmosphere. Regarding the variation with the solar cycle, the higher (lower) production of O atoms during solar maximum (minimum) conditions produce a higher (lower) value for the O/CO_2 ratio. However, the solar cycle effect over the daytime concentrations is very small, reflecting probably a more efficient depletion due to enhanced circulation during solar maximum conditions, as shown by *Bougher et al.* [1999a].

5. Day-Night and Day-to-Day Variability of Zonal Mean Temperatures

[83] As stated before, the upper atmosphere presents a strong day night cycle, that can dominate over other variations, such as the vertical and latitudinal ones.

[84] This diurnal cycle at the exobase level was presented in Figure 3. It can be seen from Figure 3 that the day-to-

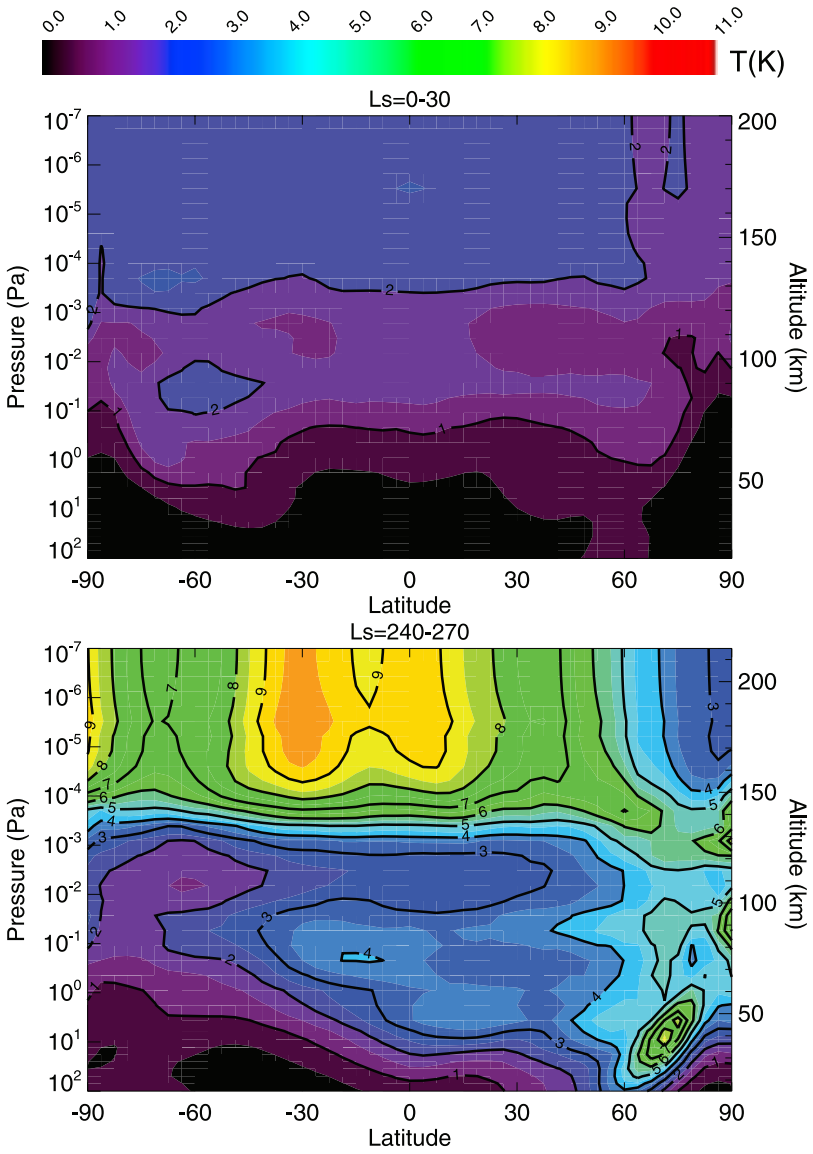


Figure 10. Zonal mean day-to-day variability RMS of the temperatures for (top) L_s = 0–30 and (bottom) L_s = 240–270.

night variation increases from aphelion, where the difference between the maximum diurnal temperature and the minimum night temperature is of about 100 K, to perihelion, where this difference can reach 200 K.

[85] We can also study the intensity of the diurnal cycle by presenting the difference of the temperature profiles at two different local times. This is presented in Figure 9 for two "months". We can see that the intensity of the diurnal cycle is much higher in the thermospheric layers, where the absorption of UV solar radiation during the day dominates the thermal balance. This thermospheric diurnal cycle is more intense during perihelion (up to 110 K day-night difference) owing to enhanced UV heating. The diurnal cycle is almost nonexistent in the polar regions owing to the special illumination conditions there.

[86] Below the thermosphere, the diurnal cycle is much less strong, reflecting the lower intensity of the heating terms dominant at these layers (absorption of IR radiation) and the effect of IR cooling, which is very effective in buffering these temperature differences. However, the signature of propagating diurnal tides of 15–20 K amplitude can be seen, especially in the L_s = 0–30 case. These types of oscillations, with similar amplitudes, have already been observed during the Viking entries [*Seiff and Kirk*, 1977] and also by SPICAM [*Forget et al.*, 2009] and Mars Climate Sounder [*McCleese et al.*, 2008], and attributed to vertically propagating thermal tides. In particular, the shape of the maxima of temperature around 10^{-1}-10^{-2} Pa reflects the structure of the thermal tide predicted from a simplified simulation of the "Hough modes" of the atmosphere [*Zurek et al.*, 1992].

[87] The day-to-day variability predicted by the model can introduce disturbances to the diurnal cycles and to the time average results discussed above, so an estimation of its magnitude is necessary to assess how representative these temporal averages are. In Figure 10 we plot the root mean

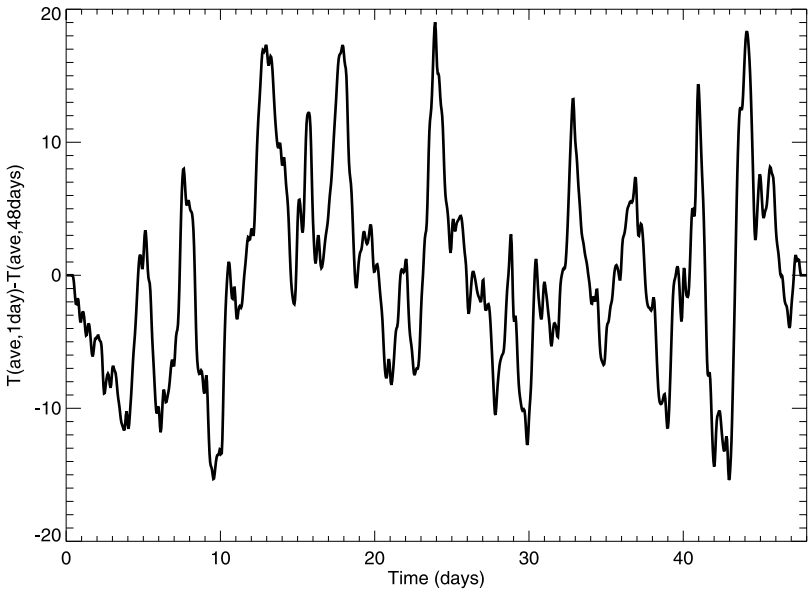


Figure 11. Temperature anomaly for fixed longitude of 120°E at the equator and at a constant pressure (10^{-6} Pa).

square of the temperature for the "months" $L_s = 0-30$ and $L_s = 240-270$, defined for each grid point as

$$T_{rms} = \sqrt{\frac{\sum_{i=1}^{N} \left(\overline{T_1}(i) - \overline{T_{10}}(i)\right)^2}{N}} \quad (9)$$

where $\overline{T_1}(i)$ and $\overline{T_{10}}(i)$ are, for each time step i in the month, the running means of the temperature over 1 and 10 days, respectively, and N the number of time steps in the "month". This procedure allows to obtain the day-to-day variability of the temperatures while removing their seasonal variability.

[88] The day-to-day variability increases with altitude, being maximum in the thermosphere. The model predicts increased variability around northern winter solstice. At this season, the variability in the lower atmosphere is especially important at the location of the eastward zonal wind jet, in the high latitudes of the winter hemisphere. It has been observed by MGS TES [*Banfield et al.*, 2004] at this particular season, at these latitudes and altitudes, an intense traveling wave activity, with an amplitude of about 12 K, in rather good agreement with the results of our model. In the upper atmosphere, the variability is more important in the low latitudes, with maximum of around 10 K. In any case, the predicted day-to-day variability is much smaller than the magnitude of the diurnal cycle.

[89] In order to elucidate the origin of these day-to-day variations in the temperatures, we have studied the temperature anomaly (i.e., the differences between a 1-day running mean temperature and the monthly mean temperature) during the $L_s = 240-270$ period. The result, for fixed longitude (120E) and latitude (the equator), is shown in Figure 11. A wave activity, with different periods between about 2 and 6 sols is observed. The maximum peak-to-peak amplitude is of about 30 K, which corresponds to the RMS of about 10 K. A Hovmoller plot (not shown) shows that these variations are longitudinally modulated by a quasi-stationary wave, with an amplitude of about 15 K and wave number 3, with maxima at longitudes 120, 0 and −120, approximately. The position of the crests and valleys of the wave shifts slowly in about 30 degrees in latitude to the west in about 45 sols. This quasi-stationary wave is also present in the monthly mean temperature, as had been previously described (at lower altitudes) by *Angelats i Coll et al.* [2004], who attributed it to nonlinear wave-wave interactions.

[90] We have studied the vertical propagation of the 2-to-6 sols wave disturbances. Some vertical propagation is observed in the low and middle atmosphere, below about 10^{-2} Pa, with the structures decreasing their pressure in a factor of 10 in about 10 days. This "slow" propagation stops at about the altitude of the mesopause. Above, the vertical propagation is almost instantaneous, so that, for a given time, the temperature structures are the same at all altitudes above about 10^{-4} Pa. This is linked to the isothermal profile imposed by a very efficient thermal conduction in the upper atmosphere, as shown before.

[91] A "real" atmosphere has other sources of day-to-day variability, like daily variations of the EUV input from the Sun. This other source is not considered at this time in our model, as only variations with the 11-year solar cycle are taken into account for the EUV solar flux.

[92] *Withers et al.* [2003] studied the day-to-day variability in the density measured during phase 2 of MGS aerobraking ($L_s \approx 50-80$). When going from a pressure layer at 10^{-3} Pa to 10^{-6} Pa, they found a decrease of the day-to-day variability, as a percentage. The observed average variability, at a constant of about 1600 LT, is of 15–20% at 130 km and 8–10% at 160 km [*Withers et al.*, 2003]. With the objective of comparing with this measurement of the day-to-day variability, we have studied the day-to-day variability of the density given by the LMD-MGCM for 1600 LT as we did before for the temperature.

[93] When expressed in percentage, the maximum variability predicted by the model varies between about 5 and

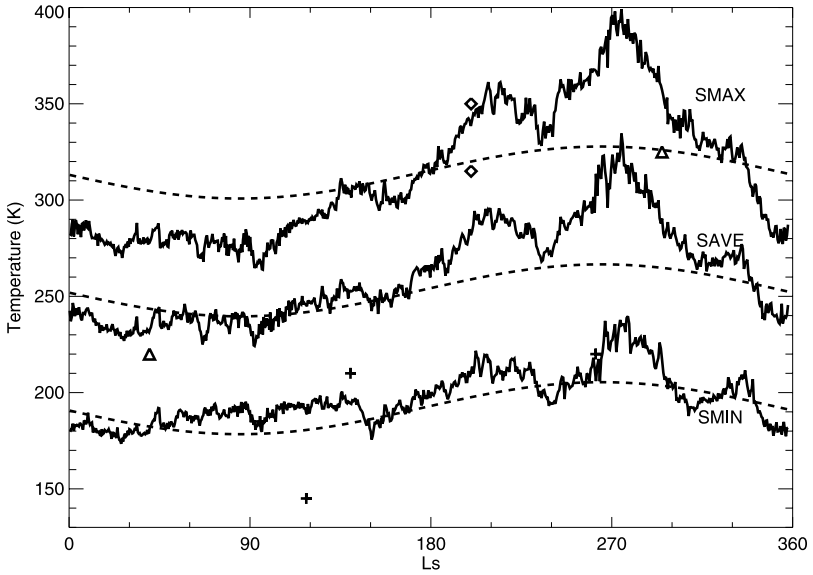


Figure 12. Seasonal variation of the LMD-MGCM longitude-averaged temperatures (K) at 45°S latitude, 10^{-6} Pa, and 1500 LT for solar maximum, average, and minimum conditions (solid lines). Curves following equation (10), taken from *Forbes et al.* [2008], for the three solar conditions (dashed lines). Symbols represent exospheric temperature measured for solar minimum (crosses for Viking Lander 1, Viking Lander 2, Mariner 4, and phase 1 of aerobraking of MGS), solar average (triangles for Mariner 9 and phase 2 of aerobraking of MGS), and solar maximum (diamonds for Mariner 6 and Mariner 7). Measured data taken from *Bougher et al.* [2000].

15% at 130 km and between 6 and 20% at 160 km. These values are of the same order of the observations by MGS, although the vertical variation of this variability is different in the model and in the observations. This can be due to the neglecting of other variability terms in the model, such as the short-term UV flux variations.

6. Variability With 11-Year Solar Cycle and Comparisons With Data

[94] The solar activity is known to vary with an average period of 11 years, as can be inferred from the observations of sunspots [*Lean*, 1987]. Although the effect over the total energy output is rather modest, there is an important wavelength dependence. The UV part of the solar spectrum is more affected, with variations of up to a factor 2 at Lyman-α [*Lean*, 1989]. Given that the UV heating is the main energy source of the upper atmosphere, a strong effect over the temperatures is expected. This solar cycle has been studied with the MTGCM [*Bougher et al.*, 2000], which predicts variations of the exobase equatorial afternoon temperature of 110 K for aphelion and 150 K for perihelion.

[95] Figure 12 shows the seasonal variation of the longitude-averaged exospheric temperatures at 45°S latitude and 1500 LT, predicted by the model for different solar conditions. The seasonal trend of increasing temperatures from aphelion to perihelion is observed in the three curves, although there are some punctual deviations, like the local maximum at $L_s \approx 150$ for solar maximum conditions. The seasonal (aphelion-to-perihelion) variation of temperatures increases with solar activity (about 60 K for solar minimum, 90 K for solar average and 120 K for solar maximum conditions). This is about 40 K higher than the seasonal variability predicted by *Bougher et al.* [2000] for a dust-free lower atmosphere. However, as stated before, a detailed comparison between these models, using similar forcings and dust loads, shows that they predict similar seasonal variations [*González-Galindo et al.*, 2006].

[96] The variation of exospheric temperatures with the solar cycle is about 100 K at around $L_s = 0$ and 150 K around perihelion, very similar to that predicted by the MTGCM [*Bougher et al.*, 2000].

[97] Following *Bougher et al.* [2000], we compare this seasonal and solar cycle variability with the scarce measurements of exospheric temperature. We have overplotted on Figure 12 the results presented in Table 1 of *Bougher et al.* [2000], using different symbols for different solar conditions: crosses for solar minimum data, triangles for solar average and diamonds for solar maximum. We have to recall that this is not a rigorous comparison, as we are not tuning the model to reproduce the different conditions for each observation. Additionally, a detailed comparison should account for the different latitudinal and local time coverage of each mission, and their variabilities when pertinent (e.g., for MGS aerobraking). The only purpose of this comparison is to estimate a grosso modo the degree of agreement of our results with the observations.

[98] In general, our model reproduces well the observed temperatures. The only exception is the Mariner 9 temperature. However, this measurement was done under a heavy dust load in the lower atmosphere, so it is not surprising that our simulation, that uses a dust scenario with no strong dust storms, underestimates the temperature in this case. This was also the case for the MTGCM [*Bougher et al.*, 2000].

[99] *Forbes et al.* [2008] have studied the variation with the solar cycle of Mars' exospheric temperatures, using data derived from precise orbit determination of MGS from 1999 to mid-2005. These temperatures are 81-day means and, owing to MGS orbital characteristics, they are equivalent to longitude averages of temperatures taken at LT 1400 and 0200, although they are strongly biased toward daytime temperatures in the southern hemisphere. So, they approximately correspond to the temperatures represented in Figure 12. *Forbes et al.* [2008] propose a fit of the variation of the exospheric temperature to the variation of L_s and solar activity of the form

$$T_\infty = 130.7 + 1.53F_{10.7} - 13.5\cos(L_s - 85) \qquad (10)$$

where T_∞ is the exospheric temperature, and $F_{10.7}$ the solar flux at 10.7 cm, used often as a proxy for EUV solar flux, corrected to account for the Mars-to-Sun distance. No significant effects of the dust distribution over the exospheric densities and temperatures is found.

[100] We have overplotted in Figure 12 three of these curves with constant values of $F_{10.7}$, in particular 40, 80 and 120, typical values for solar minimum, average and maximum activity conditions. Our model predicts well the variation of the exospheric temperatures with the solar cycle, but predicts a seasonal cycle stronger than observed by MGS [*Forbes et al.*, 2008].

[101] Sensitivity tests performed with the LMD-MGCM show that, when increasing the UV heating efficiency from the 16% value used in these simulations to a more standard 21% value [*Fox et al.*, 1996], the exospheric temperatures increase by about 15–20% [*González-Galindo*, 2006]. According to Figure 12, such an increase would make the LMD-MGCM severely overestimate the exospheric temperatures. This is the reason why we have chosen a lower value for this parameter, as stated in section 3. Although the value of the UV heating efficiency should not ideally be a tunable parameter, we have chosen to do so in this study to allow for a better reproduction of the experimental results. But clearly the thermal balance in our model has to be reviewed to address this question.

[102] We think that the overestimation of exospheric temperatures if using an appropriate value for the UV heating efficiency is related to an underestimation of the 15 μm cooling. Our parameterization uses, as stated in section 2.1, a constant atomic oxygen profile instead of the "actual" atomic oxygen concentration predicted by the model. But it is known that the collisions with atomic oxygen are very efficient in exciting the vibrational state of the CO_2 molecule. An underestimation of the atomic oxygen concentration would then lead to an underestimation of the 15 μm cooling and an overestimation of the temperatures. Tests with a 1-D model show that a correction of this problem improves the comparison with SPICAM temperatures in the mesopause and lowers considerably the thermospheric temperatures [*Forget et al.*, 2009]. We are currently working on a new version of the 15 μm cooling parameterization that will hopefully solve this problem and will allow for the use of a more correct UV heating efficiency [*López-Valverde and González-Galindo*, 2008]. This will also allow us to explore the use of a lower O-CO_2 deactivation rate, more in agreement with the experimental results [*Huestis et al.*, 2008].

7. Summary and Perspectives

[103] We have presented the extension to the thermosphere of the LMD-MGCM. Parameterizations for physical processes important in the rarefied Martian upper atmosphere have been developed and included in this GCM. This new tool is the first ground-to-exosphere Martian GCM and allows for the first time for self-consistent studies of the important couplings between different atmospheric layers and between different physical processes.

[104] We present the results of the first 1 full Martian year simulation with a GCM covering the thermosphere. In this paper we focus on the study of the solar cycle, seasonal, day-night and day-to-day variations of the temperatures in the upper thermosphere. In a companion paper, the situation during perihelion conditions is studied in more depth.

[105] The balance between the different heating/cooling terms and the implications of the values used for the UV heating efficiency and the CO_2 15 μm cooling are discussed. In order to reproduce the observed thermospheric temperatures, we need to use a UV heating efficiency lower than the standard value and a O-CO_2 deactivation rate higher than the measured value (but standard in GCM studies). We think the reason is that our CO_2 cooling parameterization does not take into account the atomic oxygen concentration predicted by the model, underestimating the cooling.

[106] The seasonal variation of the thermospheric temperature is determined by the eccentric Martian orbit, with little effect of the seasonally varying amount of dust. This seasonal variation depends also on latitude, being about 90 K (from 195 to 285 K) for the equatorial region and 140 K (from 180 to 320 K) in the south polar region, for zonal mean temperatures. This variation is around 40 K higher than observed [*Forbes et al.*, 2008] and than predicted by a dust-free MTGCM [*Bougher et al.*, 2000]. Slightly different results are found for day mean and night mean temperatures.

[107] The study of the detailed longitude-latitude distribution of the temperatures shows an important effect of the dynamics over the thermal structure. The convergence/divergence of winds produces adiabatic warming/cooling that modifies the temperature structure imposed by the radiative processes.

[108] The study of the vertical structure of the zonal mean temperatures shows a mesopause temperature between 110 and 130 K, with little seasonal variations. The pressure level of the mesopause is shown to vary between day and night and with seasons, depending on the latitude. The simulated mesopause is situated too low and is too hot when compared with SPICAM observations.

[109] We have also studied the altitude of the homopause, showing that during the solstices it is located higher in the atmosphere owing to a more effective mixing produced by a more efficient general circulation. The seasonal and solar cycle variation of the atomic oxygen relative concentration has been also analyzed. Our results are in reasonable agreement with measurements by Mariner 9 and previous results from the MTGCM.

[110] A strong day-night cycle is observed in the thermosphere owing to the absorption of UV solar radiation. The day-night temperature difference is higher during the perihelion season. Below the thermosphere, we have observed the signature of a vertically propagating diurnal tide, similar in magnitude to those observed by Viking [*Seiff and Kirk*, 1977], SPICAM [*Forget et al.*, 2009] and MCS [*McCleese et al.*, 2008].

[111] The day-to-day variability of the temperatures is found to be lower than 10%, so both the seasonal and the day-night cycles are only slightly distorted by this day-to-day variability. Wave variations with a period of 2 to 6 sols are observed. However, its origin remain uncertain. We have compared the day-to-day variability given by our model for the density with the observations of MGS [*Withers et al.*, 2003]. The overall observed magnitude of this variability is correctly reproduced by our model, although we do not reproduce its vertical variation.

[112] The predicted variation of the temperatures of the upper atmosphere with the 11-years solar cycle has been analyzed and compared with the observations and previous simulations. A good agreement with the observations is found if a 16% UV heating efficiency is used. This is lower than the 21 ± 2% theoretical value [*Fox et al.*, 1996], indicating that our model tends to overestimate temperatures in the upper atmosphere. This is probably related to the overestimation of the temperatures in the mesopause region. Comparisons with the seasonal and solar flux variation obtained from MGS precise orbit determination [*Forbes et al.*, 2008] shows that our model reproduces nicely the solar cycle variation, but it overestimates the seasonal variation of exospheric temperatures. A similar solar cycle variation of the temperatures is obtained with the MTGCM [*Bougher et al.*, 2000].

[113] This newly extended model opens new perspectives to comparisons with the most recent data from the upper Martian atmosphere. As an example, this model has already been used for analysis of SPICAM density and temperature profiles [*Forget et al.*, 2009]. The interest of these comparisons is twofold. First, they are invaluable as a validation exercise for our recently extended model. The validation and improvement of a model of this complexity is a long-lasting process fed by the necessity of analyzing and understanding new data. Second, it will allow a better understanding of the data. Aerobraking data sets are especially valuable for this task. Also, data from the Mars Express UV spectrometer SPICAM are very useful as they cover the mesosphere and the lower-thermosphere region, a very exciting region that marks the transition from the lower to the upper atmosphere. Our next step will be the study of the observed NO nightglow, that will allow to test the dynamics of the model, in particular the intensity of the interhemispheric circulation induced by the thermal tides. For that purpose, we are already working in the extension of the photochemical module to include Nitrogen compounds [*González-Galindo et al.*, 2007].

[114] Another data set covering this altitude range is the electron density profiles measured by different missions. The reproduction of the altitude and density of the ionopeaks, as well as the features of the eluding ionopause are among objectives. Our team is already working on a simplified ionospheric scheme suitable to be included in the GCM [*Gilli et al.*, 2007].

[115] In addition to including new processes, we are convinced of the necessity of improving the performance of some of the parameterizations already included in the model. This is especially necessary in view of the differences obtained when comparing with observations of the upper Martian atmosphere. So, we are currently working in the improvement of the 15 μm cooling parameterization and its description of the effect of collisions with atomic oxygen [*López-Valverde and González-Galindo*, 2008]. We hope this improvement will help to reduce significantly the temperatures above about 80 km, allowing for a better agreement with the data. Also an improvement of the NIR heating parameterization is envisaged in the near future.

[116] With these studies and theoretical developments we aim to contribute to a better understanding of this complex and fascinating region.

[117] **Acknowledgments.** M.A.L-V. was supported by Spanish Ministerio de Educacion y Ciencia under project AYA-2008-03498. The authors wish to thank two reviewers for their useful and constructive comments.

References

Anbar, A. D., M. Allen, and H. A. Nair (1993), Photodissociation in the atmosphere of Mars: Impact of high-resolution, temperature-dependent CO_2 cross-section measurements, *J. Geophys. Res.*, *98*, 10,925–10,931.

Angelats i Coll, M., F. Forget, M. A. López-Valverde, P. L. Read, and S. Lewis (2004), Upper atmosphere of Mars up to 120 km: Mars Global Surveyor data analysis with the LMD general circulation model, *J. Geophys. Res.*, *109*, E01011, doi:10.1029/2003JE002163.

Angelats i Coll, M., F. Forget, M. A. López-Valverde, and F. González-Galindo (2005), The first Mars thermospheric general circulation model: The Martian atmosphere from the ground to 240 km, *Geophys. Res. Lett.*, *32*, L04201, doi:10.1029/2004GL021368.

Banfield, D., B. J. Conrath, P. J. Gierasch, R. J. Wilson, and M. D. Smith (2004), Traveling waves in the martian atmosphere from MGS TES nadir data, *Icarus*, *170*, 365–403, doi:10.1016/j.icarus.2004.03.015.

Bell, J. M., S. W. Bougher, and J. R. Murphy (2007), Vertical dust mixing and the interannual variations in the Mars thermosphere, *J. Geophys. Res.*, *112*, E12002, doi:10.1029/2006JE002856.

Bertaux, J. L., et al. (2005), Nightglow in the upper atmosphere of Mars and implications for atmospheric transport, *Science*, *307*, 566–569.

Bougher, S. W., and R. E. Dickinson (1988), Mars mesosphere and thermosphere: 1. Global mean heat budget and thermal structure, *J. Geophys. Res.*, *93*, 7325–7337.

Bougher, S. W., R. G. Roble, E. C. Ridley, and R. E. Dickinson (1990), The Mars thermosphere: 2. General circulation with coupled dynamics and composition, *J. Geophys. Res.*, *95*, 14,811–14,827.

Bougher, S. W., S. Engel, R. G. Roble, and B. Foster (1999a), Comparative terrestrial planet thermosphere: 2. Solar cycle variation of global structure and winds at equinox, *J. Geophys. Res.*, *104*, 16,591–16,611.

Bougher, S. W., G. Keating, R. Zurek, J. Murphy, R. Haberle, J. Hollingsworth, and R. T. Clancy (1999b), Mars global surveyor aerobraking: Atmospheric trends and model interpretation, *Adv. Space Res.*, *23*, 1887–1897.

Bougher, S. W., S. Engel, R. G. Roble, and B. Foster (2000), Comparative terrestrial planet thermospheres: 3. Solar cycle variation of global structure and winds at solstices, *J. Geophys. Res.*, *105*, 17,669–17,692.

Bougher, S. W., S. Engel, D. P. Hinson, and J. R. Murphy (2004), MGS Radio Science electron density profiles: Interannual variability and implications for the Martian neutral atmosphere, *J. Geophys. Res.*, *109*, E03010, doi:10.1029/2003JE002154.

Bougher, S. W., J. M. Bell, J. R. Murphy, M. A. López-Valverde, and P. G. Withers (2006), Polar warming in the Mars thermosphere: Seasonal variations owing to changing insolation and dust distributions, *Geophys. Res. Lett.*, *33*, L02203, doi:10.1029/2005GL024059.

Bougher, S. W., P.-L. Blelly, M. Combi, J. L. Fox, I. Mueller-Wodarg, A. Ridley, and R. G. Roble (2008), Neutral upper atmosphere and ionosphere modeling, *Space Sci. Rev.*, *139*, 107–141, doi:10.1007/s11214-008-9401-9.

Chipperfield, M. P. (1999), Multiannual simulations with a three-dimensional chemical transport model, *J. Geophys. Res.*, *104*, 1781–1805.

Clancy, R. T., B. J. Sandor, M. J. Wolff, P. R. Christensen, M. D. Smith, J. C. Pearl, B. J. Conrath, and R. J. Wilson (2000), An intercomparison of ground-based millimeter, MGS TES, and Viking atmospheric temperature measurements: Seasonal and interannual variability of temperatures and dust loading in the global Mars atmosphere, *J. Geophys. Res.*, *105*, 9553–9572.

Cox, C., A. Saglam, J.-C. Gérard, J.-L. Bertaux, F. González-Galindo, F. Leblanc, and A. Reberac (2008), Distribution of the ultraviolet nitric oxide Martian night airglow: Observations from Mars Express and comparisons with a one-dimensional model, *J. Geophys. Res.*, *113*, E08012, doi:10.1029/2007JE003037.

Crowley, G., M. A. Bullock, C. Freitas, D. Boice, L. Young, D. H. Grinspon, R. Gladstone, R. Link, and W. Huebner (2003), Development of a surface-to-exosphere Mars atmosphere model, paper presented at Mars Atmosphere Modelling and Observations Workshop, Eur. Space Agency, Granada, Spain, 13–15 Jan.

Dickinson, R. E., and E. C. Ridley (1972), Numerical solution for the composition ot a thermosphere in the presence of a steady subsolar-to-antisolar circulation with application to Venus, *J. Atmos. Sci.*, *29*, 1557–1570.

Dickinson, R. E., and E. C. Ridley (1975), A numerical model for the dynamics and composition of the Venusian thermosphere, *J. Atmos. Sci.*, *32*, 1219–1232.

Donnelly, R. F., H. E. Hinteregger, and D. F. Heath (1986), Temporal variation of solar EUV, UV and 10830-A radiation, *J. Geophys. Res.*, *91*, 5567–5578.

Forbes, J. M., A. F. C. Bridger, S. W. Bougher, M. E. Hagan, J. L. Hollingsworth, G. M. Keating, and J. Murphy (2002), Nonmigrating tides in the thermosphere of Mars, *J. Geophys. Res.*, *107*(E11), 5113, doi:10.1029/2001JE001582.

Forbes, J. M., F. G. Lemoine, S. L. Bruinsma, M. D. Smith, and X. Zhang (2008), Solar flux variability of Mars' exosphere densities and temperatures, *Geophys. Res. Lett.*, *35*, L01201, doi:10.1029/2007GL031904.

Forget, F., F. Hourdin, R. Fournier, C. Hourdin, and O. Talagrand (1999), Improved general circulation models of the Martian atmosphere from the surface to above 80 km, *J. Geophys. Res.*, *104*, 24,155–24,175.

Forget, F., F. Montmessin, J.-L. Bertaux, F. González-Galindo, S. Lebonnois, E. Quémerais, A. Reberac, E. Dimarells, and M. A. López-Valverde (2009), Density and temperatures of the upper Martian atmosphere measured by stellar occultations with Mars Express SPICAM, *J. Geophys. Res.*, *114*, E01004, doi:10.1029/2008JE003086.

Fox, J. L., P. Zhou, and S. W. Bougher (1996), The Martian thermosphere/ionosphere at high and low solar activities, *Adv. Space Res.*, *17*, 203–218.

García Muñoz, A. (2007), Formulation of molecular diffusion in planetary atmospheres, *Planet. Space Sci.*, *55*, 1414–1425.

Gilli, G., F. González-Galindo, M. A. López-Valverde, and F. Forget (2007), First modelling of the Mars ionosphere with the European Mars GCM, paper presented at European Mars Science and Exploration Conference: Mars Express and ExoMars, Eur. Space Agency, Noordwijk, Netherlands, 12–16 Nov.

González-Galindo, F. (2006), Modelos energéticos, químicos y dinámicos de la alta atmósfera marciana, Ph.D. thesis, 343 pp., University of Granada, Granada, Spain, 2 June.

González-Galindo, F., M. A. López-Valverde, M. Angelats i Coll, and F. Forget (2005), Extension of a Martian general circulation model to thermospheric altitudes: UV heating and photochemical models, *J. Geophys. Res.*, *110*, E09008, doi:10.1029/2004JE002312.

González-Galindo, F., S. W. Bougher, M. A. López-Valverde, F. Forget, and J. Bell (2006), Thermal structure of the martian thermosphere: LMD-IAA GCM and MTGCM intercomparison, paper presented at Second Workshop on Mars Atmosphere Modelling and Observations, Eur. Space Agency, Granada, Spain, 27 Feb. to 3 Mar.

González-Galindo, F., F. Forget, and M. A. López-Valverde (2007), LMD-MGCM extended up to the thermosphere: Capability for the study of Mars Express upper atmosphere data, paper presented in European Mars Science and Exploration Conference: Mars Express and ExoMars, Eur. Space Agency, Noordwijk, Netherlands, 12–16 Nov.

Hougton, J. T. (1977), *The Physics of Atmospheres*, Cambridge Univ. Press, New York.

Hourdin, F. (1992), A new representation of the absorption by the CO2 15-microns band for a Martian general circulation model, *J. Geophys. Res.*, *97*, 18,319–18,335.

Hourdin, F., P. Le Van, F. Forget, and O. Talagrand (1993), Meteorological variability and the annual surface pressure cycle on Mars, *J. Atmos. Sci.*, *50*, 3625–3640.

Huestis, D. L., S. W. Bougher, J. L. Fox, M. Galand, R. E. Johnson, J. I. Moses, and J. C. Pickering (2008), Cross sections and reaction rates for comparative planet aeronomy, *Space Sci. Rev.*, doi:10.1007/s11214-008-9383-7.

Hunten, D. (1973), The escape of light gases from planetary atmospheres, *J. Atmos. Sci.*, *30*, 1481–1494.

Hunten, D. (2002), Exospheres and planetary escape, in *Atmospheres in the Solar System: Comparative Aeronomy*, *Geophys. Monogr. Ser.*, vol. 130, edited by M. Mendillo, A. Nagy, and J. H. Waite, pp. 171–190, AGU, Washington D. C.

Keating, G., et al. (1998), The structure of the upper atmosphere of Mars: In situ accelerometer measurements from Mars Global Surveyor, *Science*, *279*, 1672–1676.

Keating, G., M. Theriot, R. Tolson, S. Bougher, F. Forget, and J. Forbes (2003), Brief review on the results obtained with the MGS and Mars Odyssey 2001 accelerometer experiments, paper presented at Mars Atmosphere: Modelling and Observations Workshop, Eur. Space Agency, Granada, Spain, 13–15 Jan.

Keating, G. M., S. W. Bougher, M. E. Theriot, and R. H. Tolson (2007), The Mars global thermosphere measured by accelerometer facilities aboard orbiters and properties of the exosphere, paper presented at the European Mars Science and Exploration Conference: Mars Express and ExoMars, Eur. Space Agency, Noordwijk, Netherlands, 12–16 Nov.

Lean, J. (1987), Solar ultraviolet irradiance: A review, *J. Geophys. Res.*, *92*, 839–868.

Lean, J. L. (1989), Contribution of ultraviolet irradiance variations to changes in the Sun's total irradiance, *Science*, *244*, 197–200.

Lefevre, F., S. Lebonnois, F. Montmessin, and F. Forget (2004), Three-dimensional modeling of ozone on Mars, *J. Geophys. Res.*, *109*, E07004, doi:10.1029/2004JE002268.

López-Puertas, M., and M. A. López-Valverde (1995), Radiative energy balance of CO_2 Non-LTE infrared emissions in the Martian atmosphere, *Icarus*, *114*, 113–129.

López-Valverde, M. A., and F. González-Galindo (2008), Fast computation of CO_2 cooling rates for a Mars GCM, paper presented at the Third International Workshop on the Mars Atmosphere: Modeling and Observations, Lunar Planet. Inst., Williamsburg, Va., 10–13 Nov.

López-Valverde, M. A., D. P. Edwards, M. López-Puertas, and C. Roldán (1998), Non-local thermodynamic equilibrium in general circulation models of the Martian atmosphere: 1. Effects of the local thermal equilibrium approximation on thermal cooling and solar heating, *J. Geophys. Res.*, *103*, 16,799–16,811.

McCleese, D. J., et al. (2008), Observations of the Martian atmosphere with the Mars Climate Sounder, paper presented at the Third International Workshop on the Mars Atmosphere: Modeling and Observations, Lunar Planet. Inst., Williamsburg, Va., 10–13 Nov.

Montmessin, F., F. Forget, P. Rannou, M. Cabane, and R. M. Haberle (2004), Origin and role of water ice clouds in the Martian water cycle as inferred from a general circulation model, *J. Geophys. Res.*, *109*, E10004, doi:10.1029/2004JE002284.

Moudden, Y., and J. C. McConnell (2005), A new model for multiscale modeling of the Martian atmosphere, GM3, *J. Geophys. Res.*, *110*, E04001, doi:10.1029/2004JE002354.

Nair, H., M. Allen, A. D. Anbar, and Y. L. Yung (1994), A photochemical model of the Martian atmosphere, *Icarus*, *111*, 124–150.

Pätzold, M., S. Tellmann, B. Häusler, D. Hinson, R. Schaa, and G. L. Tyler (2005), A sporadic third layer in the ionosphere of Mars, *Science*, *310*, 837–839.

Ridley, A. J., G. Toth, and S. W. Bougher (2004), The Global Ionosphere Thermosphere Model and its applications to planetary atmospheres, *Eos Trans. AGU*, *85*(17), Jt. Assem. Suppl., Abstract SA42A-06.

Sander, S. P., et al. (2006), Chemical kinetics and photochemical data for use in atmospheric studies evaluation number 15, *JPL Publ., 06-2*, 523 pp.

Seiff, A., and D. B. Kirk (1977), Structure of the atmosphere of Mars in summer at mid-latitudes, *J. Geophys. Res.*, *82*, 4364–4378.

Smith, M. D. (2004), Interannual variability in TES atmospheric observations of Mars during 1999–2003, *Icarus*, *167*, 148–165.

States, R. J., and C. S. Gardner (2000), Thermal structure of the mesopause region (80–105 km) at 40°N latitude: Part I. Seasonal variations, *J. Atmos. Sci.*, *57*, 66–77.

Stewart, A. I. F., M. J. Alexander, R. R. Meier, L. J. Paxton, S. W. Bougher, and C.-G. Fesen (1992), Atomic oxygen in the Martian thermosphere, *J. Geophys. Res.*, *97*, 91–102.

Strobel, D. F. (2002), Aeronomic systems on planets, moons, and comets, in *Atmospheres in the Solar System: Comparative Aeronomy*, *Geophys. Monogr. Ser.*, vol. 130, edited by M. Mendillo, A. Nagy, and J. H. Waite, pp. 7–22, AGU, Washington D. C.

Tobiska, W. K. (2001), Validating the solar EUV proxy E10.7, *J. Geophys. Res.*, *106*, 29,969–29,978.

Tobiska, W. K., T. Woods, F. Eparvier, R. Viereck, L. Floyd, D. Bouwer, G. Rottman, and O. R. White (2000), The SOLAR2000 empirical solar irradiance model and forecast tool, *J. Atmos. Sol. Terr. Phys.*, *62*, 1233–1250.

Wilson, R. J. (1997), A general circulation model simulation of the Martian polar warming, *Geophys. Res. Lett.*, *24*, 123–127.

Wilson, R. J. (2000), Evidence for diurnal period Kelvin waves in the Martian atmosphere from Mars Global Surveyor TES data, *Geophys. Res. Lett.*, *27*, 3889–3892.

Wilson, R. J. (2002), Evidence for nonmigrating thermal tides in the Mars upper atmosphere from the Mars Global Surveyor accelerometer experiment, *Geophys. Res. Lett.*, *29*(7), 1120, doi:10.1029/2001GL013975.

Withers, P., S. W. Bougher, and G. M. Keating (2003), The effects of topographically-controlled thermal tides in the martian upper atmosphere as seen by the MGS accelerometer, *Icarus*, *164*, 14–32.

Zhao, X., and R. P. Turco (1997), Photodissociation parameterization for stratospheric photochemical modeling, *J. Geophys. Res.*, *102*, 9447–9459.

Zurek, R. W., J. R. Barnes, R. M. Haberle, J. B. Pollack, J. E. Tillman, and C. B. Leovy (1992), Dynamics of the atmosphere of Mars, in *Mars*, pp. 835–933, Univ. of Ariz. Press, Tucson.

M. Angelats i Coll, F. Forget, F. González-Galindo, and E. Millour, Laboratoire de Météorologie Dynamique, Institute Pierre Simon Laplace, 4 Place Jussieu, Paris F-85721, France. (fgglmd@lmd.jussieu.fr)

M. A. López-Valverde, Instituto de Astrofísica de Andalucía, CSIC, Camino Bajo de Hutor 50, Granada E-18008, Spain.